Bioactive Materials 25 (2023) 399–414

Contents lists available at ScienceDirect

Bioactive Materials

journal homepage: www.keaipublishing.com/en/journals/bioactive-materials

A biomimetic piezoelectric scaffold with sustained Mg^{2+} release promotes neurogenic and angiogenic differentiation for enhanced bone regeneration

Liangyu Wang [a], Yanyun Pang [b], Yujing Tang [c], Xinyu Wang [a], Daixing Zhang [a], Xu Zhang [b], Yingjie Yu [a,**], Xiaoping Yang [a,d], Qing Cai [a,*]

[a] State Key Laboratory of Organic-Inorganic Composites; Beijing Laboratory of Biomedical Materials, Beijing University of Chemical Technology, Beijing, 100029, China
[b] School and Hospital of Stomatology, Tianjin Medical University, Tianjin, 300070, China
[c] SINOPEC (Beijing) Research Institute of Chemical Industry Co., Ltd., Beijing, 100013, China
[d] Foshan (Southern China) Institute for New Materials, Foshan, 528200, Guangdong, China

ARTICLE INFO

Keywords:
Bone regeneration
Piezoelectricity
Neurogenic
Angiogenic
Osteogenic

ABSTRACT

Natural bone is a composite tissue made of organic and inorganic components, showing piezoelectricity. Whitlockite (WH), which is a natural magnesium-containing calcium phosphate, has attracted great attention in bone formation recently due to its unique piezoelectric property after sintering treatment and sustained release of magnesium ion (Mg^{2+}). Herein, a composite scaffold (denoted as PWH scaffold) composed of piezoelectric WH (PWH) and poly(ε-caprolactone) (PCL) was 3D printed to meet the physiological demands for the regeneration of neuro-vascularized bone tissue, namely, providing endogenous electric field at the defect site. The sustained release of Mg^{2+} from the PWH scaffold, displaying multiple biological activities, and thus exhibits a strong synergistic effect with the piezoelectricity on inhibiting osteoclast activation, promoting the neurogenic, angiogenic, and osteogenic differentiation of bone marrow mesenchymal stromal cells (BMSCs) *in vitro*. In a rat calvarial defect model, this PWH scaffold is remarkably conducive to efficient neo-bone formation with rich neurogenic and angiogenic expressions. Overall, this study presents the first example of biomimetic piezoelectric scaffold with sustained Mg^{2+} release for promoting the regeneration of neuro-vascularized bone tissue *in vivo*, which offers new insights for regenerative medicine.

1. Introduction

Bone regeneration is a complex process which involves neuron formation, angiogenesis, and osteogenesis [1,2]. At the initial stage of bone defect repair, the lack of blood vessel limits nutrition and oxygen supply, thus compromising cell proliferation and tissue regeneration [3]. Furthermore, since bone is a kind of neuro-vascularized tissue, neurogenesis is also crucial for its regeneration [4–6]. It has been reported that nerve cells secrete neuropeptides, such as calcitonin gene-related polypeptide (CGRP), which can activate CGRP receptors in osteoblasts to induce osteogenic differentiation [7,8]. Therefore, in addition to osteoinductivity, materials that could simultaneously promote neuron and blood vessel formation are highly desired for bone tissue engineering [9].

Natural bone tissue is a heterogeneous material consisting of inorganic minerals and organic collagen [10,11]. The minerals are mainly calcium and phosphorus in the form of hydroxyapatite (HA, $Ca_{10}(PO_4)_6(OH)_2$) [12]; while it is usually doped with rich Mg^{2+} to form a fraction of whitlockite (WH, $Ca_{18}Mg_2(HPO_4)_2(PO_4)_{12}$) [13], which displays attractive features in bone development due to the versatile biofunctions of Mg^{2+} [14–16]. Moreover, the assembled collagen/HA composite endows natural bone tissue with piezoelectric properties, presenting piezoelectric coefficient (d_{33}) of 0.7–2.3 pC/N [17], which is an essential factor in governing cell proliferation, migration, and differentiation [18]. It has been reported that the reconstruction of the physiological electrical microenvironment at defect sites *via* the application of piezoelectric materials is an effective strategy to enhance ossification, particularly, providing instructive cues at the initial stage of osteogenesis [19,20]. Notably, neurogenesis can also benefit from this strategy due to the conductive nature of nerve tissue [21].

Peer review under responsibility of KeAi Communications Co., Ltd.
* Corresponding author.
** Corresponding author.
E-mail addresses: yuyingjie@mail.buct.edu.cn (Y. Yu), caiqing@mail.buct.edu.cn (Q. Cai).

https://doi.org/10.1016/j.bioactmat.2022.11.004
Received 8 October 2022; Received in revised form 5 November 2022; Accepted 12 November 2022
Available online 29 November 2022

Capitalizing on this, tremendous efforts have been devoted toward the development of piezoelectric scaffold in tissue engineering. A biomimetic scaffold that emulates both the composition and piezoelectric properties of natural bone provides a promising strategy for regenerative medicine; however, the major challenge here is the choice of a proper piezoelectric material to satisfy the diverse demands during the regeneration process [22,23]. For biomedical applications, conventional piezoelectric materials can be classified into inorganic materials (*i.e.*, barium titanate ($BaTiO_3$) [24,25], potassium sodium niobate (KNN) [26–28], boron nitride (BN) [29], *etc.*) and polymeric materials (*i.e.,* polyvinylidene fluoride (PVDF) [30], *etc.*). $BaTiO_3$ and PVDF are the most widely used piezoelectric materials to promote bone regeneration, nevertheless, they are poorly degradable materials, which raise concerns for their *in vivo* implantation, that necessitates a second surgery after the tissue repairing [31,32]. Furthermore, due to the lack of bioactive factors, current piezoelectric scaffolds cannot simultaneously induce angiogenesis and neurogenesis [33,34], which make them hard to achieve satisfactory repair of critical-sized bone injures. Thus, it is of great significance to combine bioactivity (*e.g.* angiogenesis) with piezoelectricity, where synergistic effects are expected to promote the regeneration of neuro-vascularized bone tissue.

Herein, we developed a versatile biomimetic composite scaffold based on piezoelectric WH (PWH). WH is an excellent alternative for HA to prepare composite scaffold for bone regeneration [35]. Different from the slowly degradable HA, which can only release limited Ca^{2+} and PO_4^{3-}, the extra Mg^{2+} released from the degradable WH is a versatile therapeutic ion that enhances cell adhesion, proliferation, and migration [14–16]. The roles of Mg^{2+} in upregulating angiogenesis and osteogenesis have been well evidenced [36]. In a recent report, Mg^{2+} was also suggested contributing to neuron formation [6]. More importantly, HA has been known for its piezoelectricity (d_{33} ~ 1.5–2.4 pC/N) [37]. As a Mg-doping calcium phosphate, annealed WH also display remarkable polarization due to domain switching above the phase transition temperature, which makes PWH match well with the electroactive properties of natural bone to enhance osteogenesis [38]. Apparently, the bioactive ion release and piezoelectricity synergistically combine in this biodegradable PWH, which is superior to the conventional piezoelectric materials like $BaTiO_3$. As shown in Scheme 1, to fabricate the PWH-containing composite scaffold, melt extrusion 3D printing was employed. Poly(ε-caprolactone) (PCL), which is a biodegradable polymer commonly used in 3D printing process [39,40], was used as raw materials for the printing. The piezoelectric PCL/PWH composite scaffold (denoted as PWH scaffold for simplification) was then obtained. For comparison, the non-electroactive PCL, PCL/WH (denoted as WH scaffold for simplification), and PCL/β-TCP (β-tricalcium phosphate, denoted as β-TCP scaffold for simplification) scaffolds were similarly printed. Briefly, inorganic nanoparticles (NPs) were initially mixed with PCL to form composite filaments using a screw extruder, followed by melt printing to obtain 3D scaffolds. The PWH scaffold exhibits remarkable piezoelectricity and sustained release of bioactive ions (*i.e.*, Mg^{2+}, Ca^{2+}). Capitalizing on this synergistic effect, PWH scaffold emulates the function of natural bone in enhancing angiogenesis, promoting neuron

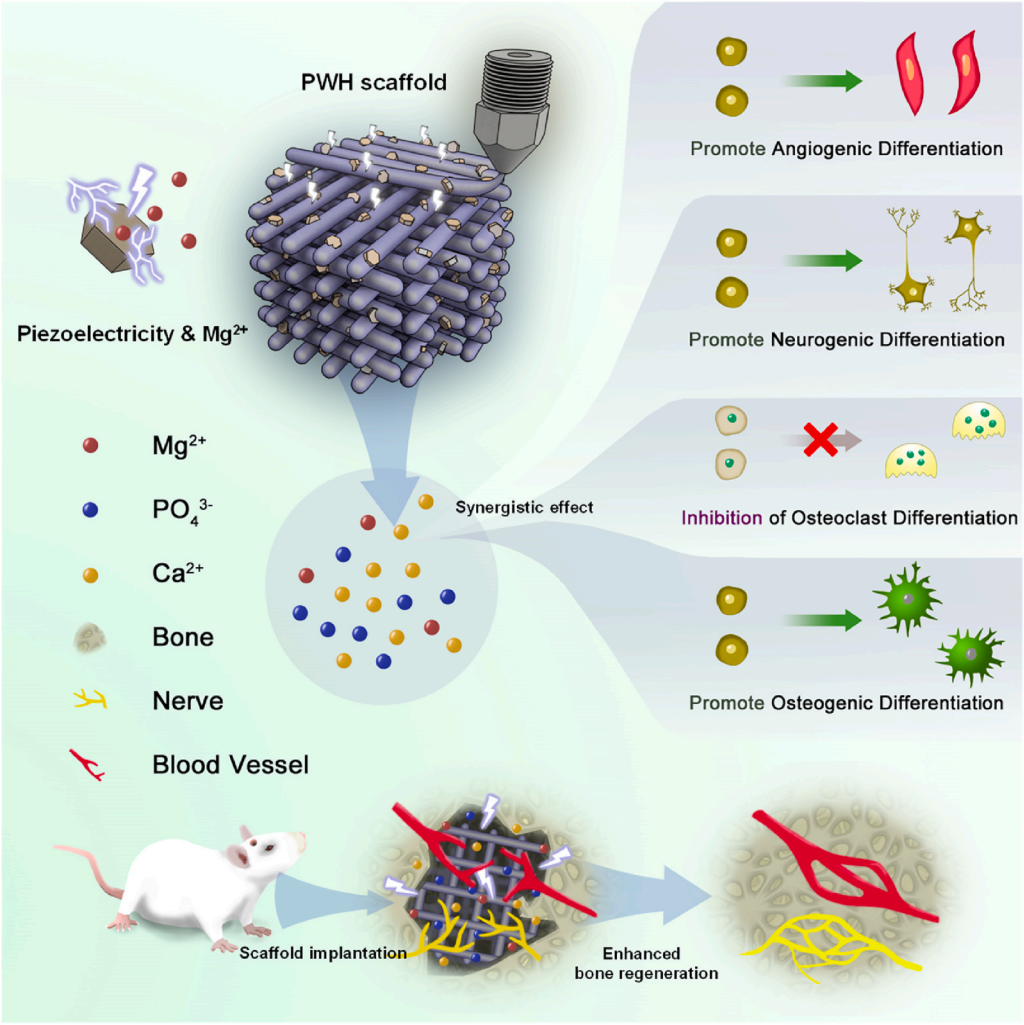

Scheme 1. Schematic illustration showing the design of the bone-specific electroactive PWH-containing organic-inorganic composite scaffold. PWH NPs are prepared from WH NPs (WH, $Ca_{18}Mg_2(HPO_4)_2(PO_4)_{12}$) after sintering, and the WH NPs are synthesized *via* chemical precipitation method. Then, PWH scaffold is prepared by 3D printing with pre-extruded PCL/PWH composite filaments. The obtained PWH scaffold exhibits robust piezoelectricity as well as sustained release of Mg^{2+} to mimic the composition and electroactivity of natural bone. A rat calvarial defect model is established for *in vivo* evaluation of neurogenesis and angiogenesis associated with neo-bone formation.

differentiation, inhibiting osteoclast activation, eventually augmenting osteogenesis. Compared to other scaffolds, such features endow the PWH scaffold with strong capacity in promoting the regeneration of neuro-vascularized bone *via in vivo* evaluations using a rat calvarial defect model. Overall, this bone-specific electroactive PWH-containing composite scaffold offers an integrated and efficient strategy for ossification.

2. Materials and methods

2.1. Chemicals and materials

PCL (M_W = 80,000) was purchased from Sigma-Aldrich (USA). Compounds for WH and β-TCP NPs synthesis, including calcium hydroxide ($Ca(OH)_2$), magnesium hydroxide ($Mg(OH)_2$), phosphoric acid (H_3PO_4), ammonium dihydrogen phosphate ($(NH_4)_2HPO_4$), and calcium chloride ($CaCl_2$) were obtained from Sinopharm Chemical Reagent *Co., Ltd.* (Shanghai, China). All other reagents and solvents used were of analytical grade and supplied by Beijing Chemical Reagent *Co., Ltd.* (China).

2.2. Synthesis and characterization of WH, PWH, and β-TCP NPs

Following reference [13], WH NPs were synthesized using a chemical precipitation method *via* the reaction of $Ca(OH)_2$, $Mg(OH)_2$, and H_3PO_4 by setting their molar ratios at 0.37 : 0.13: 0.5. $Ca(OH)_2$ and $Mg(OH)_2$ were co-dissolved in deionized water and maintained at 100 °C for 0.5 h, followed by dropwise addition of H_3PO_4 solution (100 mL, 0.5 M) at a rate of 12.5 mL/min. The reaction was heated at 100 °C for 10 h and the pH of the system was maintained at 5 during the reaction. After 14 h of aging at room temperature, milky white precipitates were centrifuged (at 4000 rpm for 5 min, CENCE, H1850) and washed until neutralization. Finally, the precipitation was dried overnight at 70 °C to obtain WH NPs. To induce the piezoelectricity, WH NPs were annealed at 650 °C in muffle furnace for 3 h to obtain the PWH NPs.

β-TCP NPs were also synthesized by the chemical precipitation method *via* the reactions of $(NH_4)_2HPO_4$ and $CaCl_2$, with their Ca/P molar ratio being set as 1.5. $(NH_4)_2HPO_4$ solution (100 mL, 0.25 M) was added into the beaker, followed by dropwise addition of $CaCl_2$ solution (150 mL, 0.25 M) at a rate of 12.5 mL/min, and ammonia was used to maintain the solution pH at 8.2. The system reacted at room temperature, and the reaction stopped after all $CaCl_2$ solution was added into the beaker. The precipitates generated in the reaction were filtered, washed, and dried. Finally, β-TCP NPs were obtained by sintering the precipitation in a muffle furnace at 850 °C for 150 min.

The morphology of the NPs was observed by scanning electron microscope (SEM, JEOL, JSM-IT200, Japan). Their composition and crystalline structure were analyzed by energy dispersive spectrometer (EDS) associated with SEM observation, as well as, Fourier transform infrared spectroscopy (FTIR, Thermo Fisher, Nicolet 6700, USA) and X-ray diffraction (XRD, Rigaku, Ultima IV, Japan).

2.3. Evaluation of the electroactivity of PWH

To evaluate the electrical properties of the PWH NPs, the powder was dispersed in dichloromethane (DCM), and then mixed with PCL/DCM solution homogeneously. The suspension was cast onto glass plate to form a PCL/PWH composite film. For comparison, PCL/WH and PCL/β-TCP composite films were prepared similarly. To keep consistency with the following composite scaffold preparation, the NPs content in all the films was fixed at 30 wt%. Then, these composite films were submitted to cyclic voltammetry (CV) curve and alternating-current (AC) impedance characterizations. As shown in Scheme S1, briefly, a three electrodes system was applied for the test, including one reference electrode (Ag/AgCl, connected with blue wire), one counter electrode (Pt plate, connected with black wire), and one working electrode (the tested sample, connected with red wire). The electrodes were immersed in 30 mL H_2SO_4 (1 M) solution, with signals being collected by an electrochemical workstation (Metrohm Autolab B.V, PGSTAT 302 N, Switzerland) *via* Nova software to obtain CV curves and AC impedance values.

2.4. Fabrication and characterization of 3D printed scaffolds

3D printed composite scaffolds were prepared *via* two steps: extruding PCL/NPs composite filaments and printing. To extrude PCL/NPs composite filaments, PCL/NPs suspensions in DCM were prepared as above. PCL/NPs blends were obtained after the complete solvent removal in a vacuum oven. Then, the blends were crashed into particles, and made into filaments *via* melt extrusion (working temperature: 120 °C) in a Wellzoom B desktop filament extruder (QV513, DH374, China). The 3D model of porous scaffolds was designed by the 123D Design computer software (Autodesk, USA). Outputted files are in the gcode format. Using the fused deposition modeling (FDM) technique, PCL/NPs filaments were submitted to a FDM printer (IEMAI 3D, MAGIC-HT-L, China) to obtain 3D structured porous scaffolds by setting the printing temperature at 150 °C, the printing speed at 8 mm/s and the filling density at 50%. Based on the incorporated NPs, PCL, PCL/WH, PCL/PWH, and PCL/β-TCP scaffolds were fabricated. These scaffolds were immersed in 20 M NaOH solution for 3 h at room temperature, and then washed with deionized water to neutral for further characterizations. For simplification, hereafter, the PCL/WH, PCL/PWH, and PCL/β-TCP scaffolds were denoted as WH, PWH, and β-TCP scaffolds, respectively.

SEM was employed to observe the morphology of the extruded filaments and printed scaffolds. Meanwhile, elemental mapping was conducted with the exposure time of 120 s. Thermogravimetric analysis (TGA, Q-50, USA) was used to evaluate the practical contents of the inorganic components in the composite scaffolds by heating the samples in air from room temperature to 650 °C at a heating rate of 10 °C/min. Water contact angle was measured by an automatic contact angle meter (SL200 A/B/D, Solon Tech., China). The volume of water droplets was 1–2 μL. After images being captured, the baseline and vertex of the water droplet bottom were found, and the value of the contact angle was automatically calculated using the software provided by the meter. Compression test on these scaffolds was carried out on a general material testing machine (Instron 5500R, UK), equipped with a 500 N load cell. The cross-head speed was set as 1 mm/min, and the total strain was set as 30% of the scaffold height.

2.5. Ion release test

To study the ion release behaviors of various composite scaffolds, each scaffold (30 mg) was immersed in 10 mL PBS at 37 °C for 21 days. At predetermined intervals, the liquid was submitted to inductively coupled plasma-optical emission spectroscopy (ICP-OES, PerkinElmer, Optima 7000DV, USA) for ion (Mg^{2+}, Ca^{2+}) concentration analysis, and 10 mL of fresh PBS was replenished to continue the release test. Three parallel measurements were conducted for each sample at each time point for averaging.

2.6. Biocompatibility study

2.6.1. Cell viability

Circular scaffolds with diameter of 6 mm and height of 0.6 mm were sterilized by being soaked in 75% ethanol for 4 h with the UV exposure, which were ready for use after PBS washing. According to standards of ISO 10993 and GB/T 16886.5, L929 fibroblasts are the suggested cell line for biocompatible evaluation of *in vivo* implants. Then, at first, scaffold extracts were prepared following these standards, that 0.2 g scaffold was soaked in 1 mL growth medium at 37 °C for 24 h, and the medium was then collected for L929 fibroblasts (Purchased from

Chinese Academy of Medical Sciences) culture after filtration. L929 fibroblasts (2×10^3) were seeded into each well of a 96-well tissue culture polystyrene (TCPs) plate. The supplement of various scaffold extracts were conducted 2 h later to allow cell attachment. On day 1, 3, 5, and 7, CCK-8 solution (10% dilution, Sigma-Aldrich, USA) was added into each well, and the plate was placed in incubator for 2 h, followed by solution absorbance recorded at 450 nm on a microplate reader (Bio-Rad 680, USA). At day 5 and 7, the cells on plates were stained with calcein-AM/PI double staining kit (Solarbio, China). Fluorescent images were captured with confocal laser scanning microscope (CLSM, TCS SP8, Leica) to evaluate their Live/Dead status (Green fluorescence: live; Red fluorescence: dead).

Next, bone marrow mesenchymal stromal cells (BMSCs) isolated from Sprague-Dawley (SD) rats were used for *in vitro* experiments. The cells were cultured in α-modified Eagle's medium (α-MEM, HyClone, USA) containing 10% (v/v) fetal bovine serum (FBS, Gibco, USA) and 1% (v/v) penicillin/streptomycin (Sigma, USA). The cells were incubated at 37 °C under saturated humidity supplied with 5% CO_2. BMSCs at passage 3 were used in the following studies, and in all the cultures, the media were refreshed every 2 days.

Then, the sterilized scaffolds were placed into the wells of a 96-well plate. BMSCs (2×10^3) were seeded onto each scaffold, supplemented with 200 μL α-MEM, and then cultured for 7 days. At predetermined intervals, CCK-8 assay was conducted to evaluate cell proliferation. At day 3, the cell/scaffold complexes were stained with calcein-AM/PI double staining kit, and observed with CLSM for Live/Dead assay.

2.6.2. Cell adhesion

BMSCs were seeded on various scaffolds at a density of 4×10^4 cell/scaffold. After being cultured for 3 and 5 days, nucleus and F-actin staining were performed. Briefly, cells on scaffolds were first fixed with 4% paraformaldehyde solution (Solarbio, China) for 1 h. After being washed with PBS, the complexes were permeabilized with 0.1% Triton X-100 for 10 min, followed by being blocked with 1% BSA solution for 30 min. Then, FITC-labeled phalloidin (Sigma-Aldrich, USA) was added to stain F-actin at room temperature for 1 h. Subsequently, DAPI was added for nucleus staining. The morphology of cytoskeleton was observed with CLSM.

2.7. Differentiation evaluations

2.7.1. Neurogenic differentiation

BMSCs were seeded on scaffold (diameter: 15 mm and height: 0.6 mm) in 24-well plate at a density of 3×10^4 cell/scaffold. At day 2, the media were replaced with neural induction medium, which was prepared by adding 50 ng/mL NGF-β (MedChemExpress, USA) into the proliferation medium. After 14 days of neurogenic inductive culture, 1 mL of Trizol RNA extract kit (Invitrogen, Carlsbad, CA) was added into each well to extract the total RNA for quantitative reverse transcription polymerase chain reaction (qPCR) assay in ABI PRISM 7500 Real-Time PCR system (Applied Biosystems, USA). Three genes (nestin, NEFL, and TUBB3) related to neurogenic differentiation were evaluated by $2^{-\Delta\Delta Ct}$ method using a housekeeping gene GAPDH as reference, and their specific primers were designed as listed in Table S1.

2.7.2. Angiogenesis assay using chicken embryo chorioallantoic membrane model

Fertilized chicken embryos were pre-incubated at 37 °C for 3 days under 60% humidity. Then, the air chambers of the eggs were carefully opened to expose the allantoic membrane. To evaluate the formation of blood vessel, various scaffolds or the extracts made from these scaffolds were placed onto the allantoic membrane or injected into the allantoic cavity. The egg opening was closed with sealing film, and incubated for another 5 days. After that, the allantoin membranes were collected and fixed with methanol/acetone (50/50) solution. The membranes were kept in PBS and visualized on a stereomicroscope (VISION, TY10Mantis Elite, Korea). Tubular length, size, and the total junction numbers of the formed blood vessels were quantitatively analyzed by AngioQuant software (Version 1.33, Mathwork Inc, Houston, TX, USA).

2.7.3. Osteogenic differentiation study

BMSCs were seeded on scaffolds (diameter: 15 mm and height: 0.6 mm) in 24-well plate at a density of 3×10^4 cell/scaffold and osteogenic induction medium was added to replace the medium in the well after one day of cell attachment and spreading, and then the inductive culture was continued for 21 days. The osteogenic induction medium was prepared by adding vitamin C (25 mg), β-glycerophosphate (1.0802 g) and dexamethasone (100 nM) into growth medium (500 mL). At day 3, 7, 14, and 21, the medium in each well was discarded. Cell lysate was obtained by adding 200 μL of cell lysis containing 1% Triton X-100, 20 mM Tris, and 150 mM NaCl, followed by five freezing-thawing circles. The activity of alkaline phosphatase (ALP) and collagen type I (COL-I) were detected by ALP assay kit (Sigma, USA) and COL-I ELISA kit (BlueGene, China), respectively. For ALP staining, BMSCs were incubated with the various scaffolds for 5 days. At day 7 and 14, the scaffolds were taken out, and the cells remained on tissue culture plates were treated with 4% paraformaldehyde (1 h) and stained with an ALP color development kit (Beyotime, China). Photos of these stained samples were taken by an optical microscope (CKX-41, Olympus, Japan).

qPCR assay was carried out at day 3, 7, and 14, 1 mL of Trizol RNA extract kit (Invitrogen, Carlsbad, CA) was added into each well to extract the total RNA for qPCR assay. Three osteogenesis-related genes (BMP-2, COL-I, and OCN) and two angiogenesis-related genes (Ang-1 and VEGF) were evaluated, and their specific primers were listed as Table S2.

2.7.4. Study on osteoclastic differentiation of RAW264.7

RAW264.7 cells (Purchased from Chinese Academy of Medical Sciences) were seeded on scaffolds (diameter: 15 mm and height: 0.6 mm) in a 24-well plate at 1×10^4 cell/scaffold. Group 1 was the control group without scaffold and added high-sugar conditioned DMEM (control group, Hyclone, USA), while Groups 2–6 were added 100 ng/mL RANKL (receptor activator of nuclear factor-κB-ligand).

Five days after RANKL induction, RAW264.7 cells were characterized with TRAP (tartrate-resistant acid phosphatase) staining (Solarbio, China) and TRAP assay kit (Beyotime, China). Meanwhile, cell morphology was visualized by the nucleus and F-actin staining. Three osteoclast-related genes (TRAP, Cathepsin K, and MMP9) were evaluated by qPCR using the specific primers listed in Table S3.

2.8. In-situ bone regeneration study

2.8.1. Scaffold implantation and micro-CT imaging

All animal experiments reported herein were performed under guidelines evaluated and approved by Animal Ethical Committee of the Academic Medical Center at Tianjin Nankai Hospital (NKYY-DWLL-2020-178 Tianjin, China). Sixteen male SD rats (200–250 g) were used to establish a critical size ($\varphi = 5$ mm) skull defect model. The rats were randomly divided into 4 groups with different scaffolds being implanted: (1) PCL, (2) β-TCP, (3) WH, and (4) PWH. To prepare the defect for scaffold (diameter: 5 mm and height: 0.8 mm) implantation, rats were shaved and anesthetized with 1% sodium pentobarbital. Then, a trephine drill bit was used to create two circular 5 mm defects separately at the bilateral region of the calvaria sagittal suture. After the implantation of scaffolds, the overlying tissues were sutured.

Two rats in each group were sacrificed at 4 W and 8 W post-implantation. The skull specimens were collected and fixed in 10% neutral buffered formalin for 12 h. Quantum GX Micro-CT (PerkinElmer, Waltham, USA) was used to scan and analyze all samples. The software provided by Quantum GX Micro-CT Workstation was used for 3D reconstruction and quantitative analysis. The region of interest (ROI) was defined as a cylinder with a diameter of 5 mm and 1 mm height to estimate relative bone volume fraction (BV/TV) and bone mineral

density (BMD). Of note, to exclude the influence of the inorganic components in residual scaffolds on BV/TV and BMD estimations, we set a density threshold (grey value) to distinguish the scaffold framework and the newly formed bone in reconstructing the images, since the composite scaffolds have higher density than the immature neobone tissue. Briefly, micro-CT images were imported into a professional medical imaging software (Mimics Medical v 17.0), and the threshold (approx. 800) was obtained with the aid of the profiling function of Mimics to mask the composite scaffold framework from bone tissue observation (Fig. S1). Thermal imaging map was generated by IRW software using the SKY mode, and drawn by setting the CT value range between 0 and 2000 [41,42].

2.8.2. Histological and immunohistological assessments

After the micro-CT analysis, the mineral in the skull was removed with a rapid decalcifier-solution (Zhongshan Goldenbridge, China). The

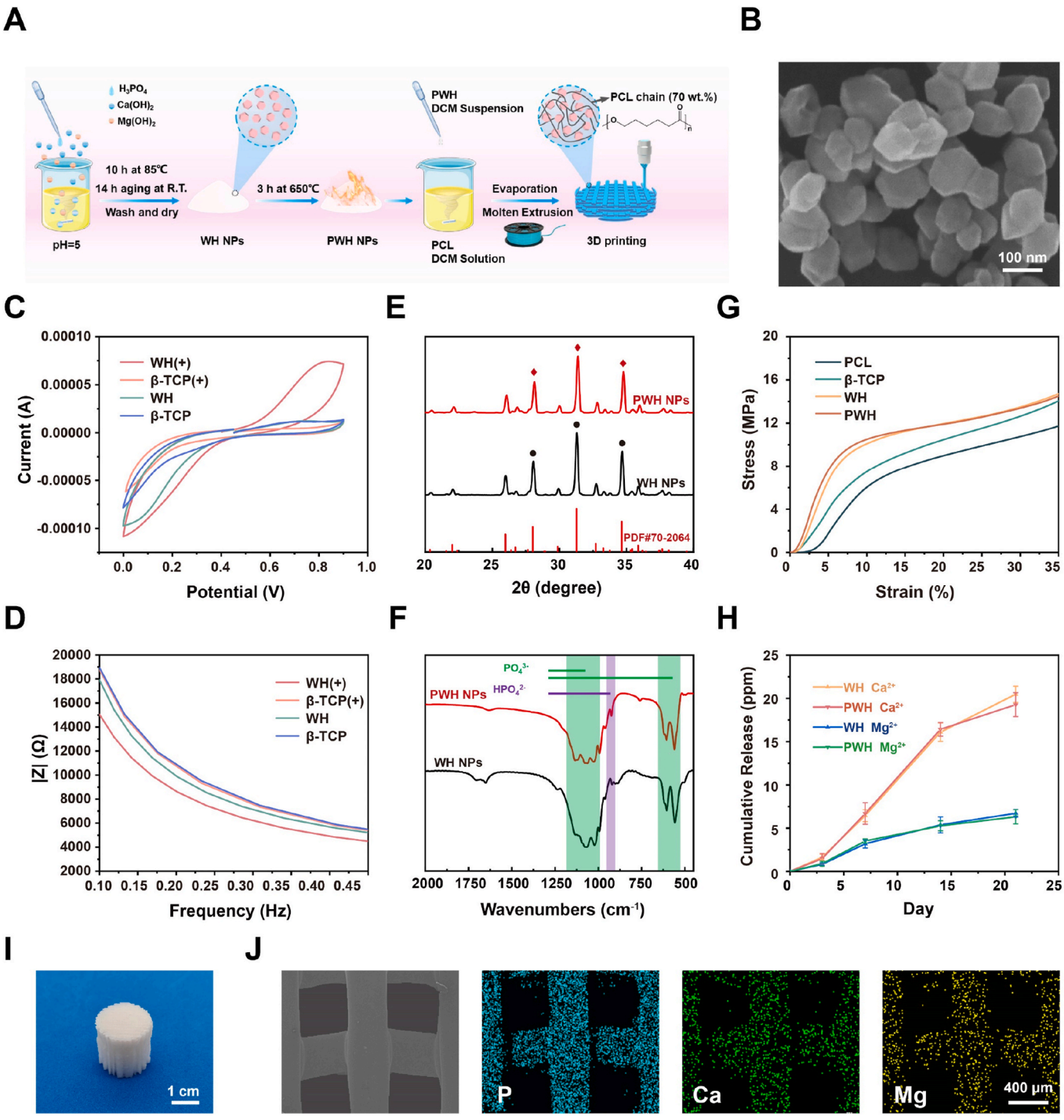

Fig. 1. Preparation and characterization of PWH NPs and PWH composite scaffolds. (A) Schematic showing the fabrication process of 3D printed composite scaffold based on PWH NPs. (B) The representative SEM image of WH NPs. (C) CV curves and (D) AC impedance curves of various composite films (± represents annealing or not). (E) XRD patterns and (F) FTIR spectra of WH NPs before and after the annealing treatment (650 °C, 3 h). (G) Compression stress-strain curves of various scaffolds. (H) Mg^{2+} and Ca^{2+} release profiles of PWH and WH scaffolds. (I) The photograph of the 3D printed PWH scaffold. (J) Representative SEM and elemental mapping images showing the morphology of the printed strands in the PWH scaffold and the even distribution of characteristic P, Ca, and Mg signals.

skull was embedded in paraffin and prepared into 3 μm-thick sections for histological, immunofluorescence, and immunohistochemistry staining assessment. Hematoxylin-eosin (H&E) and Masson's trichrome (Senbeijia, China) staining were performed on consecutive tissue sections, and images were collected by digital slice scanning equipment (Hamamatsu Nanosomer, Japan).

For immunohistochemical evaluation, TRAP (Absin, abs136593) and OCN (Beyotime, AF6297) were used as primary antibodies. Antigen retrieval was completed by incubation with 0.4% pepsin at 37 °C for 15 min. Endogenous peroxidase was blocked by 3% H_2O_2. Non-specific protein binding was blocked by 1% BSA solution. The sections were incubated with primary antibodies for 3 h at room temperature. Then the sections were incubated with secondary antibodies for 1 h at room temperature. Finally, the color was developed using a DAB substrate kit, and the optical microscope was used to take photographs.

For immunofluorescence evaluation, CD31 (Affinity, AF6191) and CGRP (Solarbio, K009774P) were used as primary antibodies. Antigen retrieval was completed by incubation with 0.4% pepsin at 37 °C for 15 min. Slices were immersed in 0.1% Triton-X 100 solution for 10 min and washed three times with PBS. The slices were incubated with 1% BSA solution for 1 h to block the binding of non-specific proteins. The sections were incubated with primary antibodies for 12 h at 4 °C, then incubated with secondary antibodies for 1 h at room temperature. Finally, the section was incubated at room temperature for 5–10 min after adding DAPI, and the fluorescence development was observed under CLSM.

2.9. Statistical analysis

All quantitative data were expressed as mean ± standard deviation (SD) for $n \geqq 3$. Statistical analysis was carried out using one-way analysis of variance (ANOVA) with Tukey's test. Differences between groups of $^*p < 0.05$ were considered statistically significant, $^{**}p < 0.01$ and $^{***}p < 0.001$ was considered highly significant. All statistical analysis was performed using SPSS 17.0 software.

3. Results

3.1. Fabrication and characterization of 3D printed scaffolds

In this study, we developed an organic-inorganic composite scaffold with piezoelectricity as well as sustained release of bioactive ions (*i.e.*, Mg^{2+}, Ca^{2+}) *via* melt extrusion 3D printing. As shown in Fig. 1A, using the chemical precipitation method, WH NPs were first synthesized by reacting $Ca(OH)_2$, $Mg(OH)_2$, and H_3PO_4. Then, WH NPs were annealed at 650 °C for 3 h to enable domain switching, which achieves the piezoelectric properties. Based on the standard XRD patterns, we confirmed that the crystalline structures of WH and β-TCP are similar (WH: PDF#70–2064; β-TCP: PDF#09–0169). For comparison, β-TCP NPs were also synthesized *via* chemical precipitation method by reacting $(NH_4)_2HPO_4$ with $CaCl_2$, and annealed using the same parameters. Therefore, the differences in the piezoelectricity and Mg^{2+} component between the PWH NPs and β-TCP NPs provide a reasonable base to identify the unique contributions of PWH in neuro-vascularized bone regeneration.

Next, the morphology and the composition of WH NPs were investigated using SEM. Fig. 1B shows a SEM image of the prepared WH NPs, displaying rhomboid morphology with average particle size of approx. 85 nm. β-TCP NPs present spherical shape with diameter of ~300 nm. EDS was then employed to investigate their compositions (Fig. S2). The spectra confirm the presence of Ca and P element in both WH and β-TCP NPs, while Mg element can only be found in WH NPs. The doping amount of Mg in the WH NPs was estimated as Mg/Ca molar ratio approx. 0.135, which is approximately consistent with the theoretical value (~0.11, $Ca_{18}Mg_2(HPO_4)_2(PO_4)_{12}$).

We continued to evaluate the electroactivity of WH and β-TCP. It should be noted that no change in electrical characterizations has been found on the β-TCP NPs before and after the annealing treatment; conversely, significant piezoelectricity has been induced to the WH NPs after annealing at 650 °C for 3 h. For the electroactive characterization, we prepared PCL composite films containing 30 wt% of various inorganic NPs *via* solution casting. The obtained composite films were submitted to CV and AC impedance measurements. In Fig. 1C, CV curves show that with the annealing treatment, an obvious redox peak at 0.8 V can be observed for the PCL/PWH film; however, all the other composite films do not display any redox peak. In addition, decreased AC impedance was identified for the PCL/PWH film in comparison with those of other films (Fig. 1D). The composition of the WH NPs synthesized *via* chemical precipitation is in the form of $Ca_{18}Mg_2(HPO_4)_2(PO_4)_{12}$. At the annealing temperature, the WH NPs tend to lose a fraction of H_2O, which results in partial reorientation of HPO_4 and PO_4 domains; this is considered as the major factor in the generation of piezoelectricity in the case of polarized HA [37]. Obviously, β-TCP NPs ($Ca_3(PO_4)_2$) do not have such characteristics. Since natural bone inherently exhibits piezoelectricity, promisingly, piezoelectric PWH NPs show advantages over WH NPs and β-TCP NPs in regenerating bone tissue for their capacity in restoring the local endogenous electric microenvironment [31,32].

To determine the influence of the partial H_2O loss on the chemical and crystalline structure of PWH, we employed XRD and FTIR to compare the subtle difference between the WH NPs and PWH NPs. From Fig. 1E, it is identified that their XRD patterns are similar, both resembling with the existing data PDF#70–2064. These results suggest that the slight domain switching alongside H_2O removal upon annealing treatment does not change the major crystalline structure of WH. The diffraction peaks locating at 28.02°, 31.28°, and 34.64° are ascribed to the crystal planes (2 1 4), (0 2 10), and (2 2 0) [43], respectively. Accordingly, no obvious variation is detected in the FTIR spectra of WH NPs and PWH NPs. As shown in Fig. 1F, they both present the characteristic peaks of PO_4^{3-} (1150-970 cm^{-1}, 604 cm^{-1}, and 558 cm^{-1}) and HPO_4^{2-} (921 cm^{-1}) [44,45]. These results confirm that the annealing process at 650 °C endow the PWH NPs with remarkable electroactivity without damaging the inherent nature of WH NPs.

Then, the next step is to fabricate porous scaffolds with piezoelectricity for implantation. Melt extrusion 3D printing was used to prepare composite scaffolds with the PWH NPs. To facilitate the printing, biodegradable PCL was selected as the biocompatible polymeric matrix due to its low melting point (approx. 60 °C) [39] and easy blending with inorganic NPs. Before printing, PWH composite filaments were first obtained *via* melt extrusion at 120 °C, whose morphology was observed using SEM and elements (P, Ca, and Mg) distribution were characterized with mapping (Fig. S3). The composite filaments are uniform with even distribution of PWH NPs. Thereafter, the filaments were used to print the PWH composite scaffold at 30 wt% addition amount of PWH NPs (Fig. 1I). As depicted in the corresponding SEM and mapping images, the printed strands are stacked to construct the porous structure, showing homogeneous P, Ca, and Mg signals resembling the strand morphology (Fig. 1J). The obtained PWH scaffold reasonably has similar piezoelectricity as the PCL/PWH film, because the molten temperature in scaffold fabrication is much lower than the sintering temperature for WH NPs. For the following comparative studies on their biological functions, WH and β-TCP scaffolds were fabricated similarly (30 wt%), as well as, pure PCL scaffold was also printed as controls. TGA was carried out to verify the incorporated amounts of different NPs. The results show that the weight remaining fractions of PWH, WH, and β-TCP scaffolds after thermal decomposition are approx. 26.7 wt%, 30.3 wt%, and 27.9 wt%, respectively, showing no significant difference to cause possible uncertainty in biological evaluations (Fig. S4). In addition, compression test was conducted on all the printed scaffolds (Fig. 1G). Among them, obviously, the pure PCL scaffold has the lowest mechanical strength. The β-TCP scaffold shows slightly inferior compressive strength to the two (P)WH-containing scaffolds, which was suggested due to the larger

β-TCP NPs size than the (P)WH NPs. It is well known that the stiffness of matrix (scaffold) has significant effects on cell spreading, migration, proliferation, and differentiation [46,47]. In our case, however, the mechanical properties of the four developed scaffolds are within the same range. Therefore, it is reasonable to rule out the mechanical factor in evaluating their biological responses, while focusing on their differences in composition and electroactivity.

WH contains bioactive elements, which is crucial for tissue regeneration. Hence, we continued to monitor the Mg^{2+} and Ca^{2+} release properties of (P)WH-containing scaffolds by immersing them into PBS. As expected, both (P)WH-containing scaffolds exhibit the sustained release of Mg and Ca ions for up to 21 days, with the accumulated concentrations at around 6.3 ppm and 19.3 ppm (Fig. 1H). Notably, the annealing treatment does not compromise the ion release properties of the scaffolds. Overall, the abovementioned results collectively demonstrate that PWH scaffold exhibits superior piezoelectricity and sustained release of bioactive ions, which is expected to be beneficial for bone regeneration.

3.2. *In vitro* biocompatibility evaluation of scaffolds

Before applying these scaffolds for cell seeding, they were slightly etched with NaOH solution at room temperature to increase surface hydrophilicity. The scaffolds made of the hydrophobic PCL present water contact angles >75°, which drop a bit with the addition of inorganic NPs (Fig. S5). After the etching, however, the water contact angles decrease to approx. 30°, and the surface roughness of the strands increases at the same time. The saponification reaction of PCL with NaOH can break the polyester chain, generating a portion of hydrophilic carboxyl and hydroxyl groups, and leading to surface erosion. It has been commonly accepted that a substrate containing functional groups and rough surface favors cell attachment and growth as compared to a hydrophobic smooth surface [48]. Thus, all the printed scaffolds have been ready for *in vitro* and *in vivo* evaluations.

Following the preparation, the biocompatibility and cell affinity of scaffolds were evaluated *via* cell proliferation using CCK-8 assay and fluorescent (Live/Dead, cytoskeleton) staining observed with CLSM. At first, according to ISO standard 10993, we prepared extracts from the scaffolds and incubated L929 fibroblasts in the extracts for the CCK-8 assay and Live/Dead staining. From Fig. 2A and S6, continuous cell growth could be observed in all the extracts. No obvious difference could be observed between different groups. The proliferated L929 fibroblasts were stained green (*i.e.,* being alive) in major, suggesting that no ingredient dissolving out of the scaffolds is cytotoxic. We continued to seed BMSCs on the scaffolds and conducted CCK-8 assay to quantify cell proliferation. As shown in Fig. 2B, the BMSCs grow well on all the scaffolds with good biocompatibility and no toxicity. In CLSM images, all the groups show majorly green fluorescence, hence suggesting the excellent biocompatibility of all the scaffolds (Fig. 2C). Overall, these results collectively demonstrate that the piezoelectric PWH scaffold shares similar behavior in cell proliferation as compared to the β-TCP and WH scaffolds. Judging from the intensity of the green fluorescence, the three composite scaffolds are more conducive to BMSCs attaching and spreading in comparison with the pure PCL scaffold. The cell spreading status was further verified with cytoskeleton staining (Fig. 2D, Fig. S7). CLSM images show that BMSCs can attach onto all the scaffolds firmly and spread in normal spindle morphology, while the cell spreading area is smaller on the PCL scaffold than on other three composite scaffolds. Further, a supplementary video is provided to show the BMSCs adhering to the PWH scaffold vividly (Movie S1).

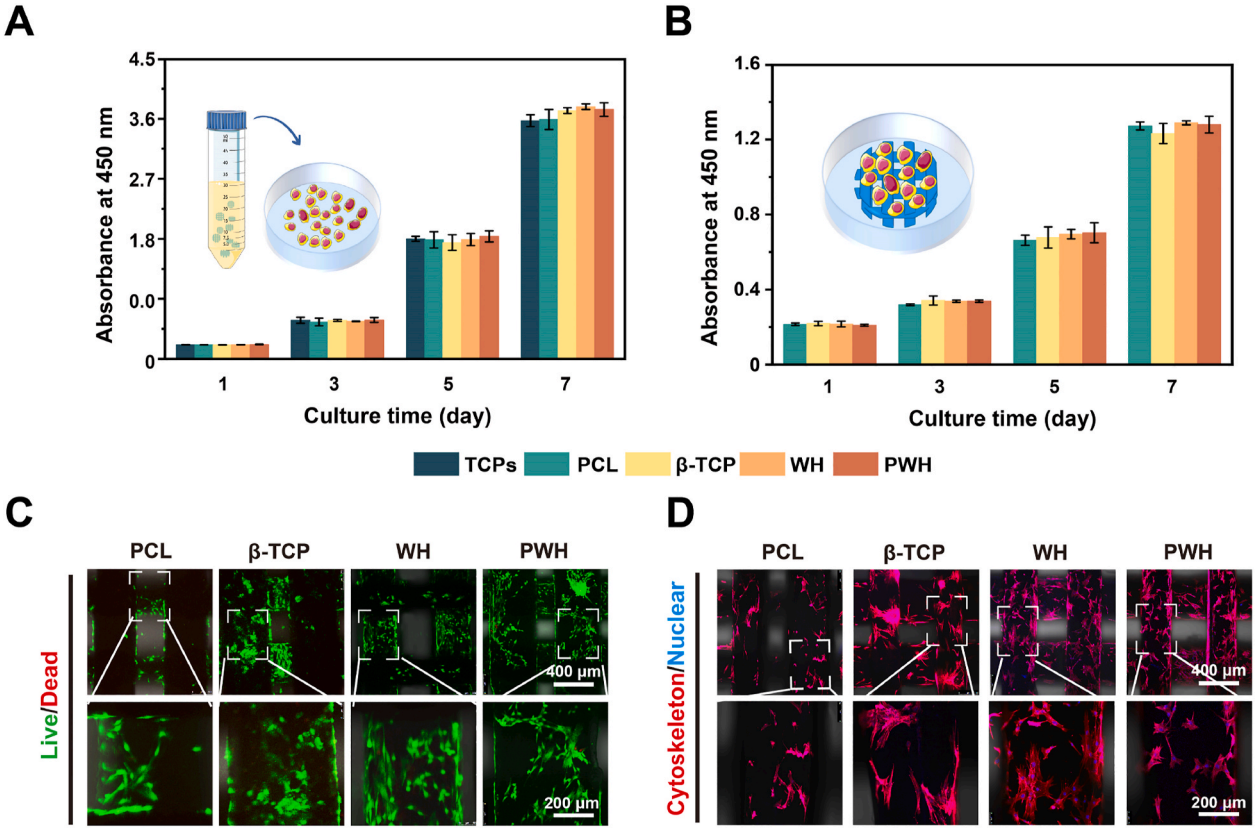

Fig. 2. Biocompatibility evaluation of various scaffolds. (A) Proliferation study of L929 fibroblasts cultured with scaffold extracts using CCK-8 assay. (B) Proliferation study of BMSCs seeded directly on various scaffolds using CCK-8 assay. (C) CLSM images show the Live/Dead staining of BMSCs cultured on various scaffolds at day 3. (D) CLSM images show the phalloidin-DAPI staining on cytoskeleton of BMSCs cultured on various scaffolds at day 3. *P < 0.05, significant, **P < 0.01 and ***P < 0.001, highly significant (n = 3).

Supplementary data related to this article can be found at https://doi.org/10.1016/j.bioactmat.2022.11.004.

3.3. Synergistic effects of Mg^{2+}/piezoelectricity on neurogenesis and angiogenesis

Bone healing is a complex signaling cascade process, which involves neural regeneration and angiogenesis as indispensable events to form neuro-vascularized bone tissue. Hence, we continued to investigate how the piezoelectricity of the PWH scaffold and its sustained release of Mg^{2+} influence these events. By directly seeding BMSCs on the scaffolds, the neurogenic and angiogenic differentiation of the cells were evaluated both quantitatively and qualitatively (Fig. 3A) [49]. For neurogenic differentiation study, real-time qPCR was applied to quantify the expressions of three related genes (nestin, TUBB3, and NEFL). It is known that nerves are electrically active tissues, and electroactive materials have a promotion effect on nerve regeneration [50–52]. As depicted in Fig. 3B, **C**, and **3D**, at day 14, the BMSCs grown on the electroactive PWH scaffold exhibit the highest gene expression level. Notably, the WH scaffold also demonstrates the capacity in upregulating the expressions of nestin, TUBB3, and NEFL genes, as compared to the PCL and β-TCP scaffolds, which show similar results to the TCPs case. This finding suggests an interesting point that the Mg^{2+} released from the WH scaffold can effectively promote neurogenesis, while the released Ca^{2+} cannot. The ability of β-TCP scaffold to upregulate the expression of neural differentiation related genes was limited. Further, the PWH scaffold has a stronger inductivity in neurogenic differentiation of BMSCs than the WH scaffold. The expression of nestin, TUBB3, and NEFL in the PWH scaffold group are 1.7, 1.3, and 1.6 times higher than that of the WH scaffold group, respectively. Apparently, such enhancement can be attributed to the synergistic effect of Mg^{2+}/piezoelectricity in the former case.

The potential of the scaffolds on angiogenesis was also characterized using qPCR analysis on gene (Ang-1, VEGF) expression for cultured

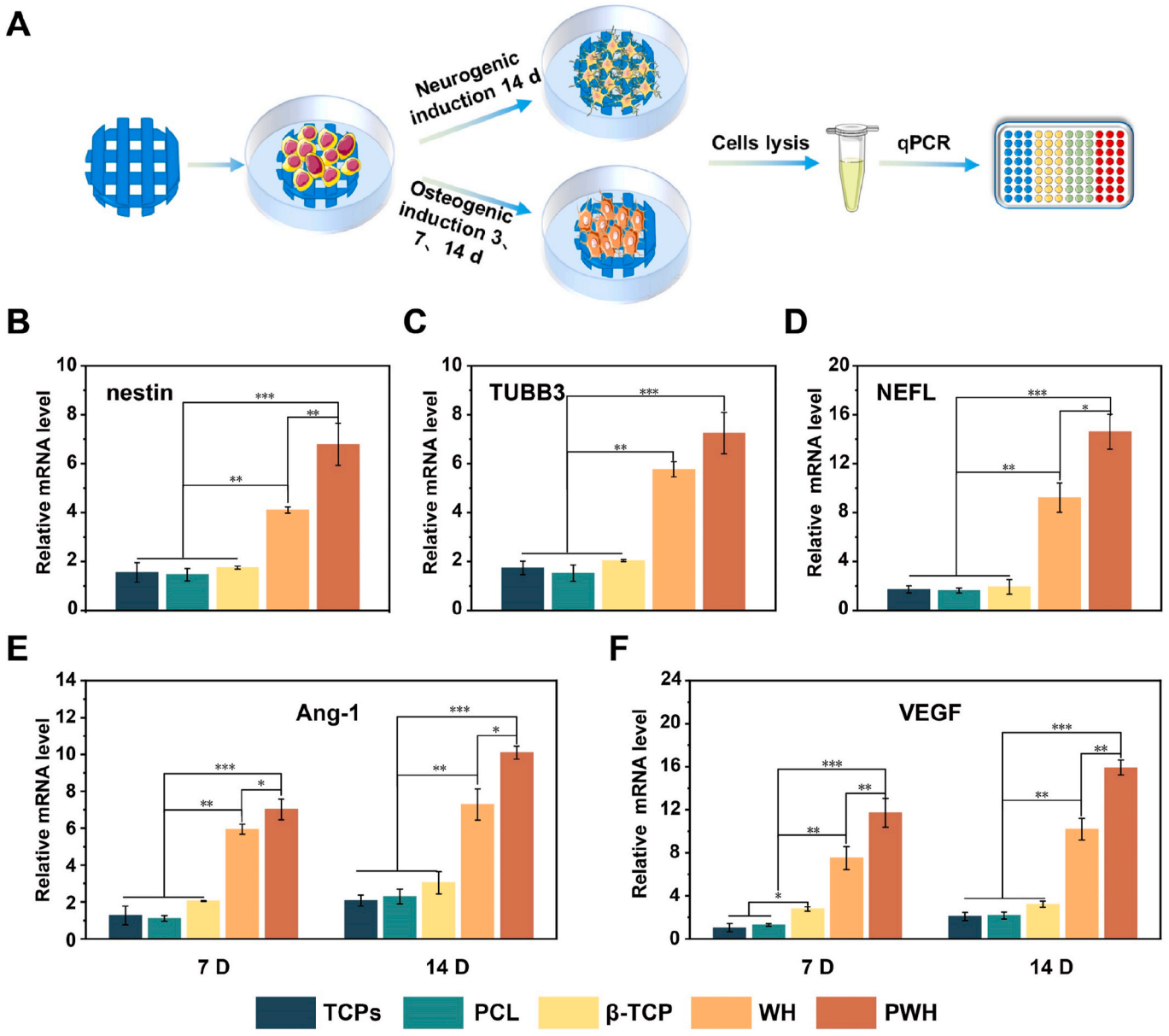

Fig. 3. Neurogenic and angiogenic differentiation of BMSCs cultured on various scaffolds. (A) A schematic showing the experimental process of RT-PCR to evaluate the neurogenic and angiogenic differentiation of BMSCs. (B–D) Effect of scaffolds on the neurogenic gene expression of BMSCs, including nestin (B), TUBB3 (C), and NEFL (D). (E, F) Effect of scaffolds on the angiogenic gene expression of BMSCs, including Ang-1 (E) and VEGF (F). *P < 0.05, significant, **P < 0.01 and ***P < 0.001, highly significant (n = 3).

BMSCs. As shown in Fig. 3E and **F,** similar to the neural differentiation results, the capacity in inducing Ang-1 and VEGF gene expression was detected decreasing gradually in the order of PWH > WH > β-TCP ≈ PCL scaffold ≈ TCPs. It has been reported that Mg^{2+} has been solidly evidenced with the capacity in promoting angiogenesis [9], while the piezoelectric scaffold that can enhance the expression of vascular-related genes is rarely reported.

We further evaluated the formation of blood vessel using the chicken embryo allantoic membrane (CAM) model (Fig. 4A) [53,54]. In one group of experimental design, the four scaffolds were directly placed on the allantoic membranes for 5 days, and photos were taken to exam the formed blood vessels invading into the areas where the scaffolds locate. As illustrated in Fig. 4B, the most abundant formation of blood vessel can be observed in the case of PWH scaffold, followed by the WH scaffold, while only limited angiogenesis is observed for both the β-TCP and PCL scaffolds. As the magnified image shown, the blood vessels have grown into the PWH scaffold. In another group of experimental design, we evaluated the angiogenesis of the extracts made from the four scaffolds. The extracts were injected onto the allantoic membranes (the control injected with PBS), which were collected for photo taken after 5 days of inoculation. The original photos are presented in Fig. 4C, together with pesudo-colored pictures to show the formation of blood vessel formation more clearly. Based on these images, quantitative analysis for vessel length, and size, and junction number was carried out using ImageJ (Fig. 4D, E and 4F). Obviously, the extracts from both the PWH and WH scaffolds display much stronger potential in inducing angiogenesis than the β-TCP and PCL scaffold groups, and the latter two share similar results to that of the control group. Of note, the PWH and WH scaffold extracts presented similar results in tubular length, vessel size, and junction formation. Taken together, the Mg^{2+} in the extracts made from the PWH and WH scaffolds is indeed playing roles in inducing angiogenesis as evidenced, which show advantages over the non-Mg^{2+} releasing scaffolds in this issue. Combined with the results shown in Fig. 3E and F, the contribution of the scaffold electroactivity on blood vessel formation can be identified as comparing the cases of PWH and WH scaffolds. Overall, it can be concluded that

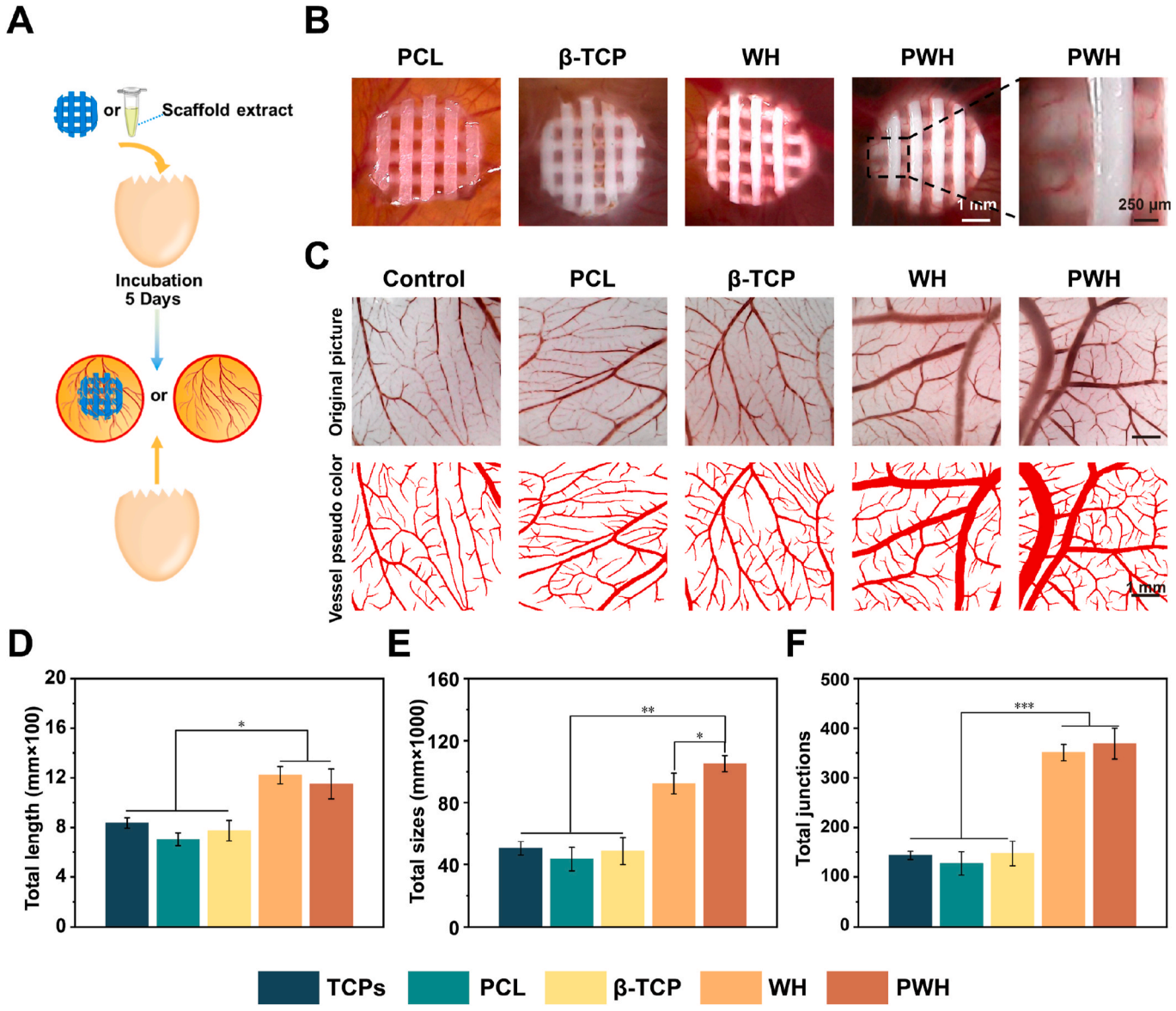

Fig. 4. Angiogenesis tested for various scaffolds using CAM assay. (A) A schematic showing the experimental process of the CAM test to visualize the angiogenesis with the stimulation directly from scaffolds or their extracts. (B, C) Representative images of blood vessel formation in the CAM test with the presence of scaffolds (B) and scaffold extracts being injected (C). (D–F) Quantification of total tubular length, vessel size, and junction numbers based on panel (C). *P < 0.05, significant, **P < 0.01 and ***P < 0.001, highly significant (n = 3).

Mg^{2+}/piezoelectricity can exert synergistic effect on promoting both neurogenesis and angiogenesis, which makes the PWH scaffold a promising choice for the regeneration of neuro-vascularized bone tissue.

3.4. Effect of scaffolds on osteogenic differentiation of BMSCs

In our scaffold design, several bioactive factors, including calcium phosphate component, Mg^{2+}-doping, and piezoelectricity, are conducive to osteogenesis. Hence, to verify the effects of the soluble ingredients (*i.e.*, the released ions) from the scaffolds on osteogenesis, BMSCs were cultured on TCPs for 7 or 14 days in the presence of various scaffolds. Then, the scaffolds were removed to characterize the BMSCs on TCPs with ALP staining [55–57]. As depicted in Fig. 5A, the staining color for the control (growth medium) and PCL groups is lighter than that in other three groups, which indicates that the released ions from β-TCP, WH, and PWH scaffolds enhanced the cellular ALP activity. As compared the β-TCP with the PWH (WH) scaffold groups, however, the ALP staining color is obviously deep in the latter two cases, confirming that the released Mg^{2+} from WH and PWH scaffolds into the media has further promoted the cellular ALP activity. Corresponding quantitative analysis for the intensity of ALP is shown in Fig. 5B, the results show that the PWH scaffold group exhibits the strongest ALP intensity compared to other groups. COL-I protein, which is a representative marker for osteogenesis, was also detected. For BMSCs seeded on scaffolds, increases in the COL-I synthesis were detected with the culture time, except the TCPs control and PCL scaffold groups (Fig. S8). The highest expression of COL-I could be found in the PWH scaffold group, followed by the WH, and then the β-TCP scaffold groups. These characterizations once again proved that the released Mg^{2+}, and its combination with scaffold electroactivity could achieve the strongest promotion effect on the osteogenic differentiation of BMSCs.

Apart from osteogenesis, maintaining of bone homeostasis is known as a dynamic process that involves a balance between bone formation and bone resorption. If osteoclasts are activated by the implanted materials, and overexpressed in comparison with osteoblasts, bone regeneration would not be satisfactory with the occurrence of significant bone resorption [58]. Piezoelectric materials have the ability to depress osteoclast phenotype, herein, we applied RAW246.7 macrophages as the osteoclastic precursor cells to test the capacity of various scaffolds in inhibiting osteoclast phenotype. To conduct the experiment, RANKL was first used to induce the osteoclastic differentiation of RAW246.7 cells, and then the cells were incubated in the presence of various scaffolds for 5 days before characterization. Similar to the ALP test, after removing the scaffolds, the RAW246.7 cells grown on the TCPs were stained to show their cytoskeleton/nuclear morphology and observed with CLSM (Fig. 6A). The RAW246.7 cells in the control group exhibit clear mononuclear morphology, and the RANKL treatment has successfully induced the formation of osteoclast-like multinucleated cells. By incubating the multinucleated cells with various scaffolds for 5 days, cell morphology changes in dependence with the scaffold properties. In the PCL and β-TCP scaffold groups, cell morphology remains similar to the RANKL induced ones; conversely, the majority of the cells in the WH and PWH scaffold groups recover to a similar morphology with the untreated RAW246.7 cells. In Fig. 6B, the results show the immunohistochemistry staining of TRAP, which is an iron-binding protein that highly expressed in osteoclasts. The deepest staining color (*i.e.*, the richest TRAP expression) can be found in the RANKL induced cells, the treatment with PCL and β-TCP scaffolds cannot change the situation, while the staining

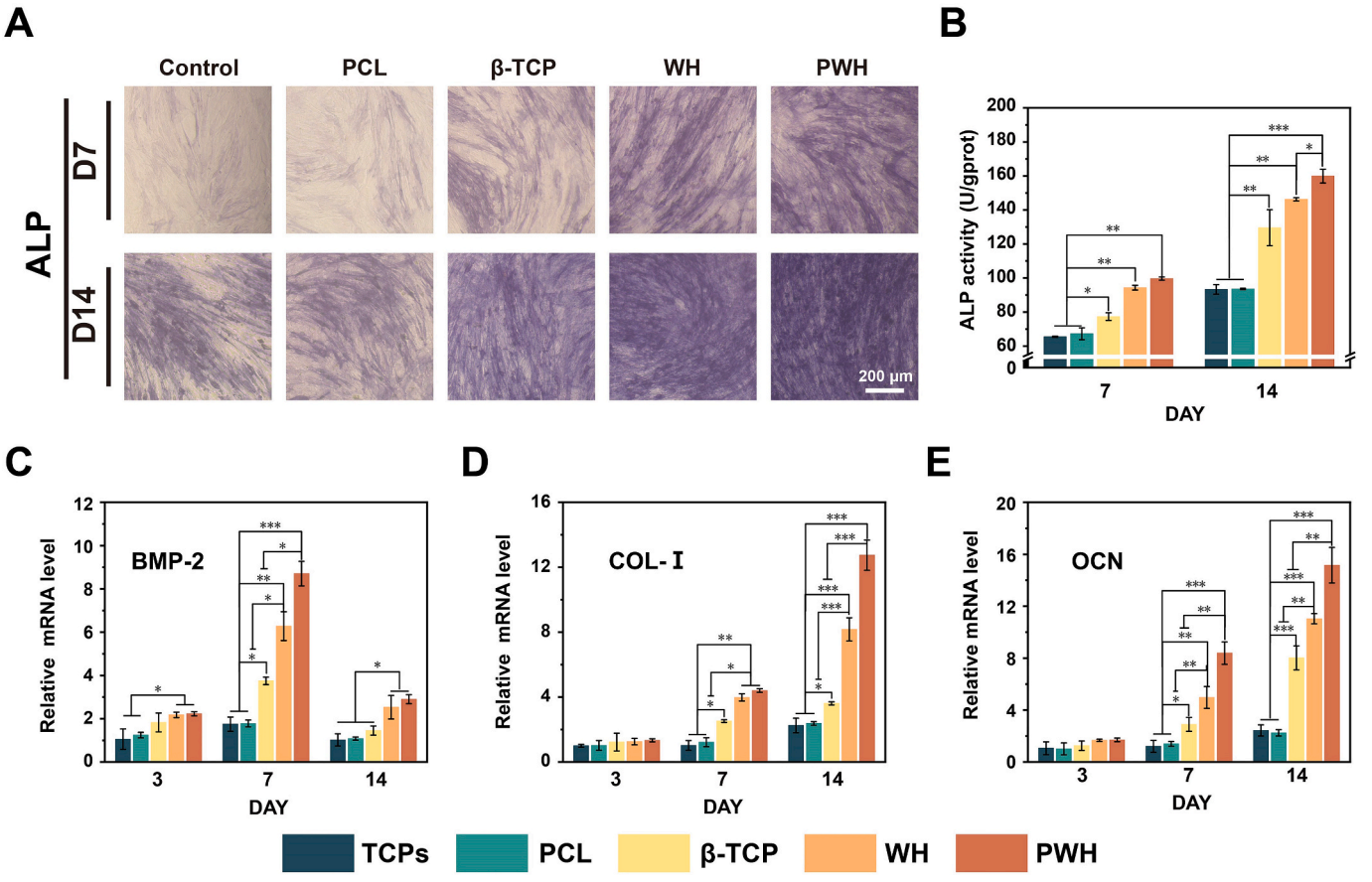

Fig. 5. Evaluations for the osteogenic differentiation of BMSCs in the presence of various scaffolds. (A) ALP staining and (B) quantified ALP activity for BMSCs cultured for 7 and 14 days. (C–E) Relative expressions of three osteogenic-related genes (BMP-2, COL-I, and OCN) detected by qPCR at day 5. *P < 0.05, significant, **P < 0.01 and ***P < 0.001, highly significant (n = 3).

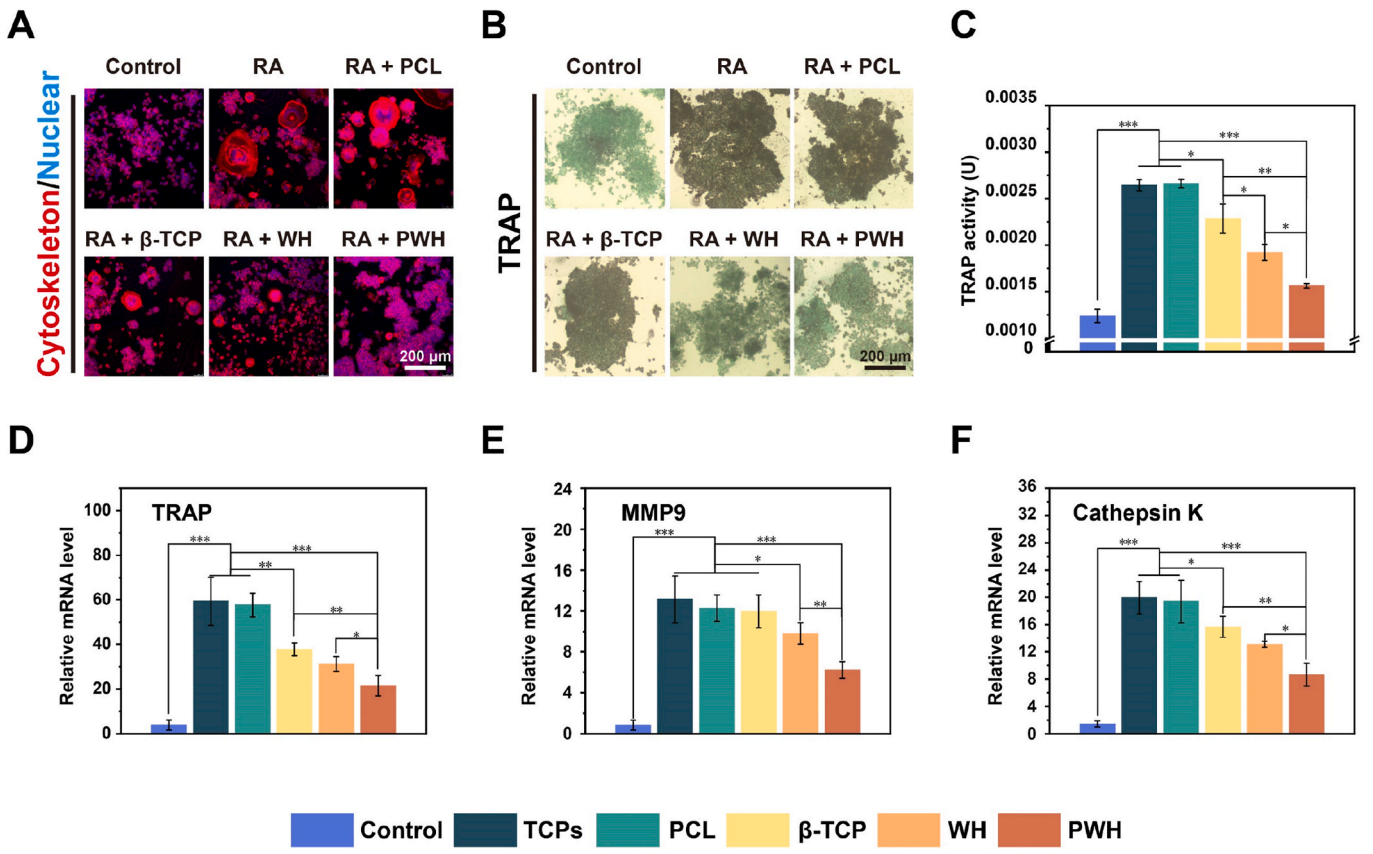

Fig. 6. Evaluation for the osteoclast differentiation of RAW 264.7 in the presence of various scaffolds. (A) CLSM images showing cytoskeleton/nucleus staining and (B) optical images showing nuclear/TRAP staining for RAW 264.7 cells induced with RANKL (shortened as RA) and further incubated with scaffolds for 5 days. (C) Quantified TRAP activity for RAW 264.7 cultured for 5 days. (D–F) Relative expressions of three osteoclastic-related genes (TRAP, MMP9, and Cathepsin K) detected by RT-PCR at day 5. *P < 0.05, significant, **P < 0.01 and ***P < 0.001, highly significant (n = 3).

color becomes lighter for the cells in the WH and PWH scaffold groups, presenting some similarity to the untreated control case. Accordingly, the quantitative data shown in Fig. 6C reveal the declining trend in TRAP activity more clearly, that the PWH scaffold can inhibit osteoclastic activation most efficiently, followed by the WH scaffold, and then the others. These findings are in accordance with the previous results of osteogenic differentiation, that the piezoelectric PWH scaffold can simultaneously achieve the promotion effect on osteogenesis and negatively influence osteoclast expression, given the fact of its sustained release of Mg^{2+} and electroactivity.

PCR analysis was further performed on the expressions of genes related to osteoblastic (BMP-2, COL-I, and OCN) and osteoclastic (TRAP, MMP9, and Cathepsin K) differentiation for BMSCs and RAW246.7 cells cultured as above, respectively. As shown in the figures, the expressions of BMP-2, COL-I, and OCN genes increase monotonically in the order of PCL < β-TCP < WH < PWH scaffold groups (Fig. 5C, **D**, and **5E**), while the expressions of TRAP, MMP9, and Cathepsin K decrease monotonically in the same order (Fig. 6D, **E**, and **6F**). The explanation for the BMP-2 achieving the highest value at day 7 is that BMP-2 is an earlier marker for osteogenic differentiation. Reasonably, the PWH scaffold is expected to achieve desirable outcomes in *in-situ* bone regeneration test, as its superior performance in regulating neurogenesis, angiogenesis, and osteoblastic/osteoclastic activity having been identified.

3.5. *In-situ* bone regeneration evaluation

Encouraged by the promising *in vitro* results, we continued to explore the capacity of the PWH scaffold in inducing *in-situ* bone regeneration using the rat calvarial defect model with a well-accepted defect size (φ = 5 mm) [59], paying attention to the neurogenesis and angiogenesis associated with neo-bone formation (Fig. 7A). At 4 W and 8 W after scaffolds being implanted, the rats were sacrificed to collect the skulls for evaluation. To view the regenerated bone tissue in the defect area, micro-CT images were taken and their corresponding heat map analysis were performed. To exclude the influence of the inorganic NPs in scaffolds on imaging and quantitative estimation, as aforementioned, a critical grey value was set to distinguish the inorganic materials in residual scaffolds and ossificated bone (Fig. S1). Therefore, from Fig. 7B, it shows that the PCL and β-TCP scaffolds barely induce the formation of neo-bone tissue, still showing a hole in the defect area after 8 W without revealing the presence of the β-TCP scaffold. Nevertheless, both the WH and PWH scaffolds induced obvious bone formation in the central region of the defects, sprouting from the defect edge and growing into scaffold framework. As expected, the most significant neo-bone formation could be observed in the PWH scaffold group. For an easy comparison, the quantitative analysis of BV/TV and BMD are shown in Fig. 7C and D. The results indicate that the PWH scaffold group exhibits the highest BV/TV and BMD among all groups, reaching 17.53% and 288.07 mg/cm^3 at 8 W post-implantation. These results obtained from the imagological examination are well consisting with the *in vitro* trends, confirming the advantages of the electroactivity and Mg^{2+}-release in osteogenesis for their bone-specific nature.

H&E and Masson's trichrome staining are the commonly used histological evaluation method to illustrate possible inflammatory response associated with scaffold implantation, as well as, to show collagen synthesis and bone maturation. The images are shown in two magnifications (Fig. 8A and Fig. S9), and no obvious inflammatory could be observed for all the groups, indicating the excellent biocompatibility of the implanted scaffolds containing various inorganic NPs. The Masson staining color is light for both the PCL and β-TCP scaffold groups, while

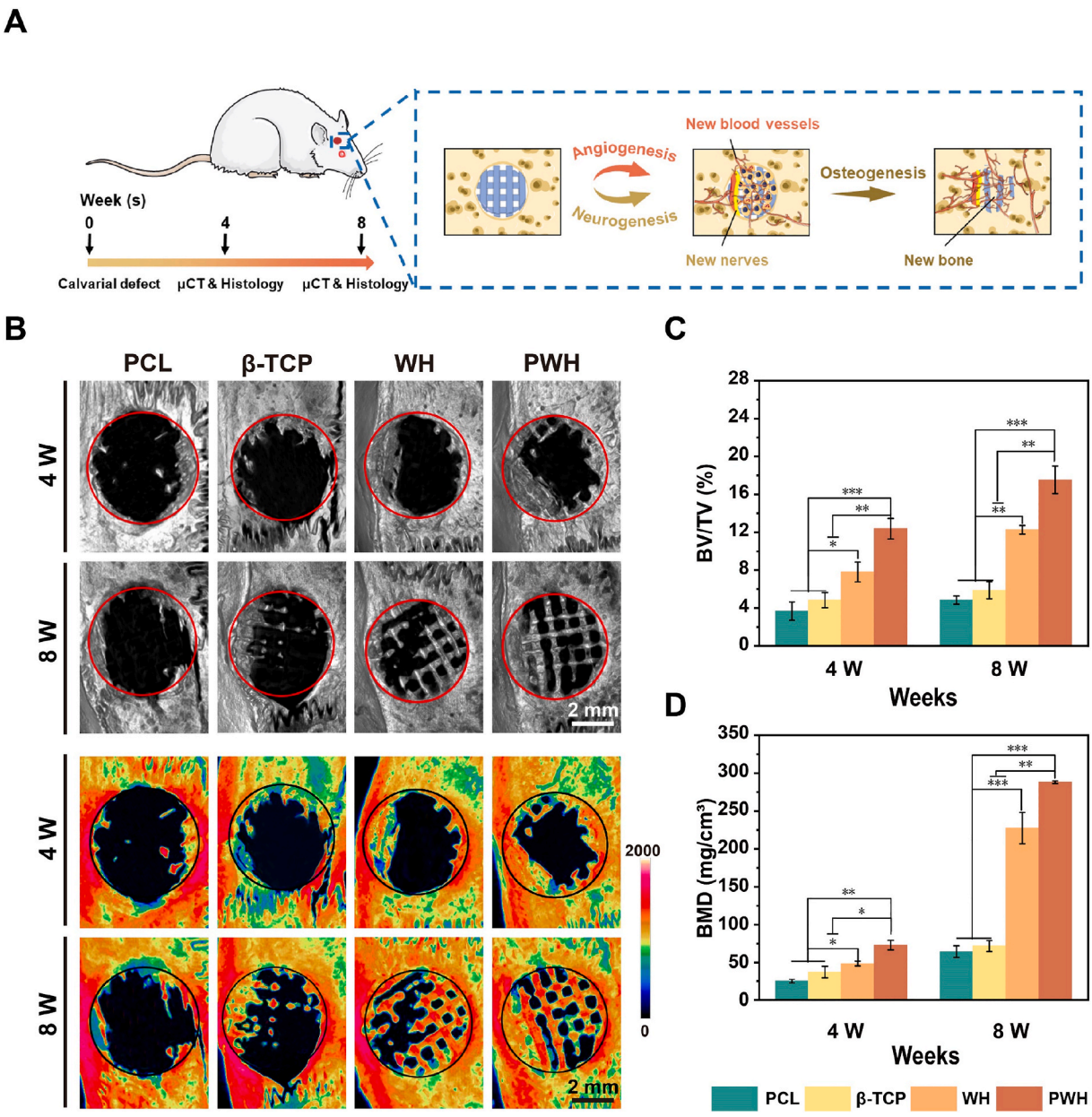

Fig. 7. The evaluation of *in-situ* bone regeneration with various scaffolds implantation. (A) A schematic showing the establishment of 5-mm skull defect model of SD rats and the mechanism for enhanced bone regeneration *via* the promoted neurogenesis and angiogenesis. (B) Reconstructed 3D micro-CT images and corresponding thermal imaging analysis of rat skulls at 4 W and 8 W post-operation. (C, D) The quantitative evaluation on regenerated bone *via* BV/TV and BMD analysis. *denotes the significant difference between PCL, β-TCP, WH, and PWH scaffold groups. *P < 0.05, significant, **P < 0.01 and ***P < 0.001, highly significant (n = 4).

the dark-blue staining in the WH and PWH scaffold groups is related to the formation of rich collagen, and the red staining indicates the organization of calcified extracellular matrix. Apparently, new bone grows into the interior of the piezoelectric PWH scaffold, while not for the PCL and β-TCP scaffolds. With limited activity in inducing osteogenesis, fibrous connective tissue (FCT) infiltrate into the PCL and β-TCP scaffolds. Differently, the spaces in the WH and PWH scaffolds, particularly in the latter case, are mainly filled with the newly formed bone tissue.

As the activation effect of the PWH scaffold on neurogenic and angiogenic differentiation of BMSCs have already been identified *in vitro*, we continued to investigate whether the scaffold could initiate similar biological events *in vivo* after implanting the scaffolds. To the end, immunofluorescence staining on CGRP (neurogenesis, green fluorescence) and CD31 (angiogenesis, red fluorescence) were carried out. As shown in Fig. 8C, the intensity of the red and green fluorescence gradually increases in the order of PCL ≈ β-TCP < WH < PWH scaffold groups, which confirms the synergistic effect of Mg^{2+} releasing and scaffold electroactivity in enhancing nerve and blood vessel formation. This trend is highly comparable with the immunohistochemical staining of TRAP (osteoclastic) and OCN (osteoblastic) expressions (Fig. 8B and Fig. S10). Hence, the WH and PWH scaffold groups present the stronger OCN and less TRAP expression than the PCL and β-TCP scaffold groups, among them, the PWH scaffold exhibits the strongest capacity in inducing osteogenesis.

4. Discussion

Physiological electrical microenvironment is a key factor in regulating proliferation, migration, and differentiation of cells, which has been extensively studied in tissue engineering including bone regeneration [18–20], while how to tune the bioelectrical cue to mediate human physiological conditions is still challenging. Various conductive and

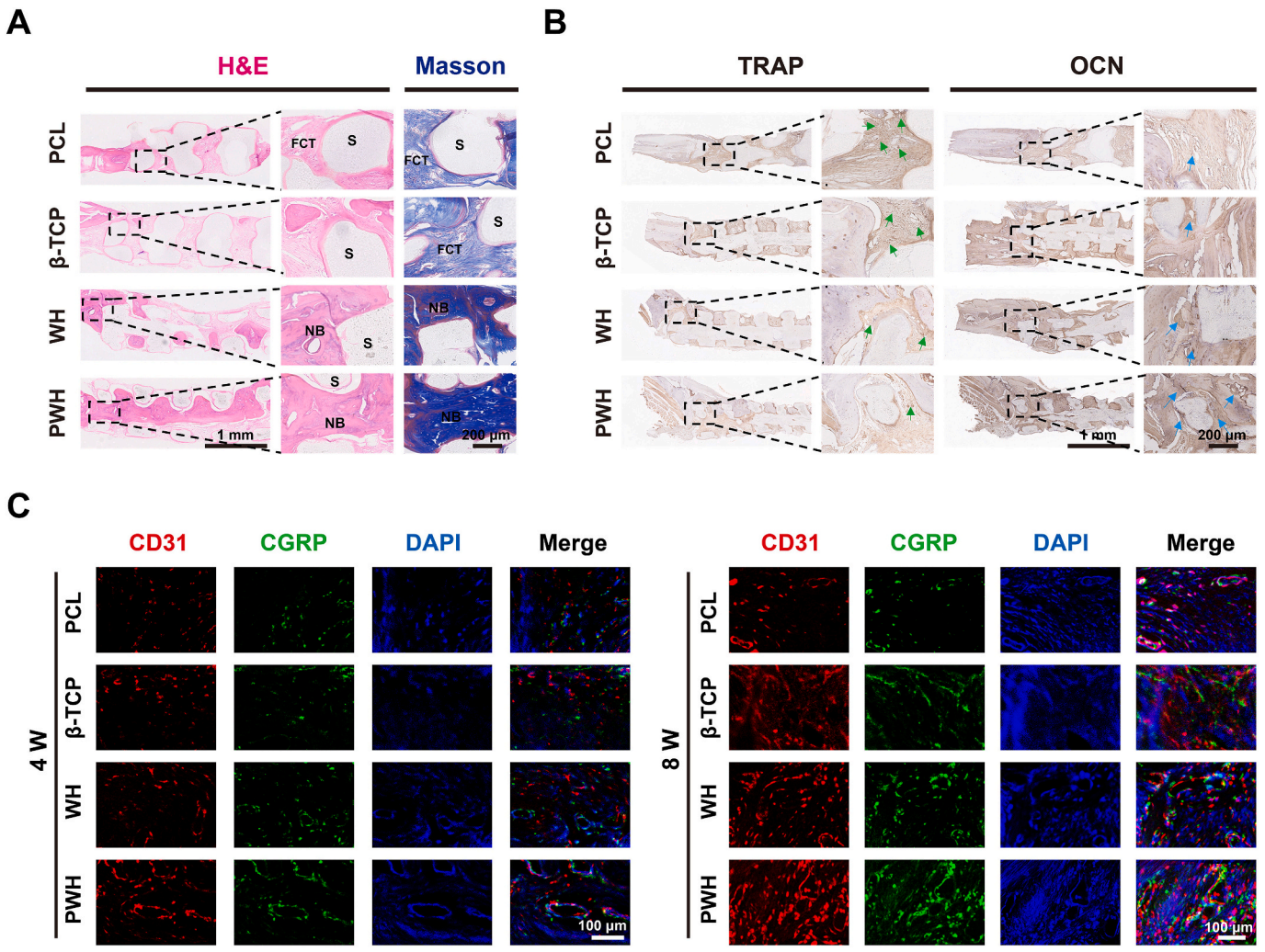

Fig. 8. Histological, immunohistological, and immunofluorescence staining for the evaluation of bone regeneration. (A) H&E staining and Masson's trichrome staining for sections collected at 8 W post-operation. (B) Immunohistochemical staining of TRAP and OCN expression at 8 W post-operation. (C) Immunofluorescence staining of CD31 (red), CGRP (green), and DAPI (blue) expression at 4 W and 8 W post-operation.

piezoelectric materials have been developed, which hold great potential for their applications in repairing injured bone tissues [24–30]. Among the electroactive materials, piezoelectric materials have drawn tremendous attention since their *in vivo* applications do not need external electric stimulus and they can directly convert mechanical pressure to the electrical signals, presenting advantages in versatility and flexibility [60]. And this is one of the major reasons for our design of piezoelectric scaffold for bone regeneration in this study.

Biodegradability is an essential property required for *in vivo* implanted scaffolds [61], while this poses challenges in the selection of piezoelectric materials because most of the currently applied piezoelectric polymers (*e.g.* PVDF) and ceramics (*e.g.* barium titanate) are non-degradable [31,32]. HA is the main inorganic component in natural bone tissue, and it is known HA presenting piezoelectricity (d_{33} = 1.5–2.4 pC/N) after properly polarization using methods like sintering and corona poling [37]. It is also known that the d_{33} of bone tissue is about 0.7–2.3 pC/N [17]. Therefore, although the piezoelecricity of HA is not as strong as $BaTiO_3$ (d_{33} ~ 190 pC/N) [62], it is compatible to the electrophysiological level of natural bone tissue, which make poled HA promote osteogenesis more profoundly than non-poled HA [63]. This finding shed light on using other types of piezoelectric calcium phosphate in inducing osteogenesis, and sintered WH turns out to be a promising choice. WH is a kind of Mg-doping calcium phosphate, which is able to gain piezoelectricity similar to HA after sintering with the water loss and crystal domain transition [38].

Herein, the sintered WH (*i.e.* PWH) NPs were incorporated into biodegradable PCL and made into porous scaffolds *via* 3D printing, thus endowing the composite scaffold with electroactivity at a proper addition amounts (30 wt% in this study). As expected, this piezoelectric PWH scaffold achieved significant promotion effect on the osteogenic differentiation of BMSCs; meanwhile, remarkable inhibition effect on osteoclastic activation, as compared to non-piezoelectric WH scaffold, confirming the important contribution of material electroactivity in upregulating events related to bone regeneration. It was further determined that inductivity on osteogenesis is in the order of PWH > WH > β-TCP > PCL. Therefore, the β-TCP scaffold behaves better than the PCL scaffold, due to the β-TCP NPs providing Ca^{2+} and phosphate ions, which are involved in calcium nodule formation [64]. Of note, what is the reason that the WH scaffold behave better than the β-TCP scaffold in enhancing osteogenesis?

Different from β-TCP, in addition to Ca^{2+} and phosphate ions, WH also provides sustained release of Mg^{2+}. It has been proven that Mg^{2+} is a multifunctional and therapeutic ion in terms of promoting cell migration, proliferation, and angiogenesis [14–16,36]. Notably, osteogenesis is a complex procedure, which is also closely related to the extent of angiogenesis, and even neurogenesis, since native bone is a kind of neuro-vascular tissue. In our results, the extracts made from the PWH and WH scaffolds displayed efficient promotion in expressions of

Ang-1 and VEGF genes in cell culture, as well as, richer formation of blood vessels in CAM assay. These finding undoubtedly demonstrate that the Mg^{2+} dissolved into the extracts is responsible for these angiogenic improvements. For assays using extracts, the PWH and WH scaffold groups present comparable outcomes, since they show similar ion release behaviors, while the scaffold piezoelectricity does not play roles in these cases.

For the enhanced neurogenesis, due to electrophysiological nature of nerve tissue, the primary promotion is originated from the electroactivity of the scaffold. As shown, the BMSCs seeded on the PWH scaffold achieves the highest expressions in nestin, TUBB3, and NEFL genes among all the groups. However, it is the WH scaffold taking the second place, being much significantly higher values in these gene expressions than the β-TCP scaffold, and the β-TCP group shares similar data with the PCL group. Based on these findings, it is proposed that the PCL itself and the released Ca^{2+}/phosphate ions have no influence in the event of neurogenesis; on the contrary, the released Mg^{2+} ion presents obvious bioactivity and is involved in the neurogenic differentiation of BMSCs. Recently, interests on neurogenesis associated with new bone formation are on the rise, for the importance of neurogenesis in the enhanced regeneration of neuro-vascularized bone tissue being gradually proved [22,65]. Various attempts were reported, among them, bioactive elements (*e.g.* Si, P, and Mg) were also involved in neurogenic events and play roles in stimulating neurogenesis [6,66,67]. Though the promotion mechanism of bioactive ions is still unclear in these reports, our findings added a solid evidence that Mg^{2+} can indeed activate neurogenesis. This is an excellent and extra cue for the PWH scaffold targeting bone regeneration, as reported, neuropeptides (*e.g* CGRP) secreted by nerve cells can activate CGRP receptors in osteoblasts to induce osteogenic differentiation [7,8].

With all these approaches from *in vitro* studies, it is highly expected that the PWH scaffold can obtain the best *in-situ* bone regeneration outcomes *via in vivo* evaluations. After the four aforementioned scaffolds being implanted in rat calvarial defect for 8 W, the highest BV/TV and BMD values are detected for the PWH group, followed by the WH group, and then the other two groups (*i,e.*, the β-TCP and PCL). The PCL polymer is non-bioactive, and the function of β-TCP is limited. The Mg^{2+}-releasing WH scaffold could induce significant neo-bone formation, while the Mg^{2+}-releasing combined with the scaffold electroactivity leads the PWH scaffold to be a promising design to restore the functions of the injured bone tissue. From the immunohistological and immunofluorescence staining results on TRAP (osteoclastic), OCN (osteoblastic), CD31 (angiogenic), and CGRP (neurogenic) in the newly formed bone tissue sections, we can conclude that the PWH scaffold exhibits the strongest capacity in manipulating these crucial events associated with ossification, which should be ascribed to the synergistic effect of piezoelectricity and Mg^{2+}. Overall, to achieve efficient bone regeneration, the piezoelectricity of implanted scaffold is not necessarily to be quite high. Efficient promotion on neo-bone formation could be achieved when the electroactive of the implanted scaffold can match well with the natural bone. With the sustained release of bioactive Mg^{2+} in upregulating angiogenesis and neurogenesis, thus, the piezoelectric PWH scaffold is much conducive to osteogenesis as evidenced.

To the best of our knowledge, this is the first time that the therapeutic effect of PWH has been comprehensively evaluated through *in vitro* and *in vivo* study. Taken together, as an endogenous bioavailable therapeutic ion, Mg^{2+} displays multiple functions in regulating cell proliferation and differentiation. The Mg-containing WH is an important inorganic component existing in natural bone tissue, which makes the WH scaffold to be more active than the β-TCP scaffold in biological events related to neurogenesis, angiogenesis, and osteogenesis due to the released Mg^{2+}. The feature that PWH NPs are piezoelectric after annealing, adds electroactivity to the PWH scaffold, which could reconstruct the local electrical microenvironment to further promote *in vivo* responses *via* mimicking the natural physiological property. In short, the piezoelectric PWH scaffold provides a comprehensive design for the *in-situ* regeneration of neurovascularizened bone tissue.

5. Conclusion

In summary, learning from the characteristics of natural bone, we presented a biomimetic scaffold mimicking the composition and piezoelectricity of the natural bone by incorporating electroactive PWH NPs *via* melt extrusion and 3D printing. The PWH composite scaffold takes advantage of the function of annealed WH NPs that can provide sustained release of bioactive ions, and exhibit piezoelectricity. The overall results of comprehensive *in vitro* experiments well demonstrated that the PWH scaffold could promote neuron differentiation, enhance angiogenesis, inhibit osteoclast, hence leading to the augmented bone regeneration. Moreover, these features make the PWH scaffold behave much better in repairing the rat calvarial defect as compared to the WH scaffold (*i.e.*, lacking electroactivity) and the β-TCP scaffold (*i.e.*, lacking both electroactivity and Mg^{2+} supply). The synergistic effect of Mg^{2+} and piezoelectricity originated from the PWH scaffold could significantly promote neurogenesis and angiogenesis for enhanced osteogenesis. Therefore, we anticipate that such a bone-specific biomimetic scaffold can offer a promising strategy towards bone regeneration, which could greatly broaden the application of WH/PWH in regenerative medicine.

Ethics approval and consent to participate

All animal experiments reported herein were performed under guidelines evaluated and approved by Animal Ethical Committee of the Academic Medical Center at Tianjin Nankai Hospital (NKYY-DWLL-2020-178 Tianjin, China).

CRediT authorship contribution statement

Liangyu Wang: Investigation, Validation, Writing – original draft. **Yanyun Pang:** Investigation. **Yujing Tang:** Validation. **Xinyu Wang:** Investigation. **Daixing Zhang:** Validation. **Xu Zhang:** Formal analysis. **Yingjie Yu:** Writing – review & editing. **Xiaoping Yang:** Supervision. **Qing Cai:** Conceptualization, Methodology, Writing – review & editing.

Declaration of competing interest

The authors declare that they have no known competing financial interests or personal relationships that could have appeared to influence the work reported in this paper.

Acknowledgements

This work was supported by the National Natural Science Foundation of China (U22A20159, 52003161), the Central Universities (buctrc202220), and the SINOPEC project (421029).

Appendix A. Supplementary data

Supplementary data to this article can be found online at https://doi.org/10.1016/j.bioactmat.2022.11.004.

References

[1] C. Wang, J. Lai, K. Li, S. Zhu, B. Lu, J. Liu, Cryogenic 3D printing of dual-delivery scaffolds for improved bone regeneration with enhanced vascularization, Bioact. Mater. 6 (2021) 137–145.
[2] H. Zheng, Y. Tian, Q. Gao, Y. Yu, X. Xia, Z. Feng, F. Dong, X. Wu, L. Sui, Hierarchical micro-nano topography promotes cell adhesion and osteogenic differentiation via integrin α2-PI3K-AKT signaling axis, Front. Bioeng. Biotechnol. 8 (2020) 463–478.
[3] H. Liu, Y. Du, G. Yang, X. Hu, L. Wang, B. Liu, J. Wang, S. Zhang, Delivering proangiogenic factors from 3D-printed polycaprolactone scaffolds for vascularized bone regeneration, Adv. Healthc. Mater. 9 (2020), 2000727.

[4] X. Wang, Y. Ma, J. Chen, Y. Liu, G. Liu, A novel decellularized matrix of Wnt signaling-activated osteocytes accelerates the repair of critical-sized parietal bone defects with osteoclastogenesis, angiogenesis, and neurogenesis, Bioact. Mater. 21 (2023) 110-128.

[5] Y. Li, D. Fraser, J. Mereness, A.V. Hove, S. Basu, M. Newman, D.S. Benoit, Tissue engineered neurovascularization strategies for craniofacial tissue regeneration, ACS Appl. Bio Mater. 5 (2021) 20–39.

[6] Y. Xu, C. Xu, L. He, J. Zhou, T. Chen, L. Yang, X. Guo, Stratified-structural hydrogel incorporated with magnesium-ion-modified black phosphorus nanosheets for promoting neuro-vascularized bone regeneration, Bioact. Mater. 16 (2022) 271–284.

[7] D. Zhang, N. Ni, Y. Su, H. Miao, Z. Tang, Y. Ji, Y. Wang, H. Gao, Y. Ju, N. Sun, Targeting local osteogenic and ancillary cells by mechanobiologically optimized magnesium scaffolds for orbital bone reconstruction in canines, ACS Appl. Mater. Interfaces 12 (2020) 27889–27904.

[8] E. Mrak, F. Guidobono, G. Moro, G. Fraschini, A. Rubinacci, I. Villa, Calcitonin gene-related peptide (CGRP) inhibits apoptosis in human osteoblasts by β-Catenin stabilization, J. Cell. Physiol. 225 (2010) 701–708.

[9] X. Ren, X. Chen, Z. Geng, J. Su, Bone-targeted biomaterials: strategies and applications, Chem. Eng. J. 446 (2022), 137133.

[10] Y. Liu, D. Luo, T. Wang, Hierarchical structures of bone and bioinspired bone tissue engineering, Small 12 (2016) 4611–4632.

[11] K.E. Stockhausen, M. Qwamizadeh, E.M. Wölfel, H. Hemmatian, I.A. Fiedler, S. Flenner, E. Longo, M. Amling, I. Greving, R.O. Ritchie, Collagen fiber orientation is coupled with specific nano-compositional patterns in dark and bright osteons modulating their biomechanical properties, ACS Nano 15 (2021) 455–467.

[12] J.A. Lett, S. Sagadevan, I. Fatimah, M.E. Hoque, Y. Lokanathan, E. Léonard, S. F. Alshahateet, R. Schirhagl, W.C. Oh, Recent advances in natural polymer-based hydroxyapatite scaffolds: properties and applications, Eur. Polym. J. 148 (2021), 110360.

[13] H.L. Jang, K. Jin, J. Lee, Y. Kim, S.H. Nahm, K.S. Hong, K.T. Nam, Revisiting whitlockite, the second most abundant biomineral in bone: nanocrystal synthesis in physiologically relevant conditions and biocompatibility evaluation, ACS Nano 8 (2014) 634–641.

[14] Y. Liu, H. Li, J. Xu, J. TerBush, W. Li, M. Setty, S. Guan, T.D. Nguyen, L. Qin, Y. Zheng, Biodegradable metal-derived magnesium and sodium enhances bone regeneration by angiogenesis aided osteogenesis and regulated biological apatite formation, Chem. Eng. J. 410 (2021), 127616.

[15] Z. Zhao, G. Li, H. Ruan, K. Chen, Z. Cai, G. Lu, R. Li, L. Deng, M. Cai, W. Cui, Capturing magnesium ions via microfluidic hydrogel microspheres for promoting cancellous bone regeneration, ACS Nano 15 (2021) 13041–13054.

[16] Z. Wan, Z. Yuan, Y. Li, Y. Zhang, Y. Wang, Y. Yu, J. Mao, Q. Cai, X. Yang, Hierarchical therapeutic ion-based microspheres with precise ratio-controlled delivery as microscaffolds for *in situ* vascularized bone regeneration, Adv. Funct. Mater. 32 (2022), 2113280.

[17] M.H. Shamos, L.S. Lavine, M.I. Shamos, Piezoelectric effect in bone, Nature 197 (1963) 81, 81.

[18] D. Khare, B. Basu, A.K. Dubey, Electrical stimulation and piezoelectric biomaterials for bone tissue engineering applications, Biomaterials 258 (2020), 120280.

[19] F. Zhao, C. Zhang, J. Liu, L. Liu, X. Cao, X. Chen, B. Lei, L. Shao, Periosteum structure/function-mimicking bioactive scaffolds with piezoelectric/chem/nano signals for critical-sized bone regeneration, Chem. Eng. J. 402 (2020), 126203.

[20] S.M. Damaraju, Y. Shen, E. Elele, B. Khusid, A. Eshghinejad, J. Li, M. Jaffe, T. L. Arinzeh, Three-dimensional piezoelectric fibrous scaffolds selectively promote mesenchymal stem cell differentiation, Biomaterials 149 (2017) 51–62.

[21] Y. Yang, H. Wang, H. Yang, Y. Zhao, J. Guo, X. Yin, Magnesium-based whitlockite bone mineral promotes neural and osteogenic activities, ACS Biomater. Sci. Eng. 6 (2020) 5785–5796.

[22] Q.Q. Wan, W.P. Qin, M.J. Shen, Y.X. Ma, B. Li, S.Y. Liu, F.R. Tay, K. Jiao, L.N. Niu, Simultaneous regeneration of bone and nerves through materials and architectural design: are we there yet? Adv. Funct. Mater. 30 (2020), 2003542.

[23] L. Zhang, Y. Yu, C. Feng, C. Chuang, X. Zuo, Y. Zhou, C. Chang, M. Simon, M. Rafailovich, Templated dentin formation by dental pulp stem cells on banded collagen bundles nucleated on electrospun poly (4-vinyl pyridine) fibers *in vitro*, Acta Biomater. 76 (2018) 80–88.

[24] T. Zheng, Y. Yu, Y. Pang, D. Zhang, Y. Wang, H. Zhao, X. Zhang, H. Leng, X. Yang, Q. Cai, Improving bone regeneration with composites consisting of piezoelectric poly(L-lactide) and piezoelectric calcium/manganese co-doped barium titanate nanofibers, Compos. B Eng. 234 (2022), 109734.

[25] K. Cai, Y. Jiao, Q. Quan, Y. Hao, J. Liu, L. Wu, Improved activity of MC3T3-E1 cells by the exciting piezoelectric $BaTiO_3$/TC4 using low-intensity pulsed ultrasound, Bioact. Mater. 6 (2021) 4073–4082.

[26] A.S. Verma, A. Sharma, A. Kumar, A. Mukhopadhyay, D. Kumar, A.K. Dubey, Multifunctional response of piezoelectric sodium potassium niobate (KNN)-toughened hydroxyapatite-based biocomposites, ACS Appl. Bio Mater. 3 (2020) 5287–5299.

[27] T. Yao, J. Chen, Z. Wang, J. Zhai, Y. Li, J. Xing, S. Hu, G. Tan, S. Qi, Y. Chang, The antibacterial effect of potassium-sodium niobate ceramics based on controlling piezoelectric properties, Colloids Surf., B 175 (2019) 463–468.

[28] W. Chen, Z. Yu, J. Pang, P. Yu, G. Tan, C. Ning, Fabrication of biocompatible potassium sodium niobate piezoelectric ceramic as an electroactive implant, Materials 10 (2017) 345–352.

[29] S.V. Anandhan, U.M. Krishnan, Boron nitride nanotube scaffolds: emergence of a new era in regenerative medicine, Biomed. Mater. 16 (2021), 044105.

[30] Y. Li, C. Liao, S.C. Tjong, Electrospun polyvinylidene fluoride-based fibrous scaffolds with piezoelectric characteristics for bone and neural tissue engineering, Nanomaterials 9 (2019) 952–961.

[31] Z. Zhang, C. Zhang, Y. Lin, P. Hu, Y. Shen, K. Wang, S. Meng, Y. Chai, X. Dai, X. Liu, Y. Liu, X. Mo, C. Cao, S. Li, X. Deng, L. Chen, Nanocomposite membranes enhance bone regeneration through restoring physiological electric microenvironment, ACS Nano 10 (2016) 7279–7286.

[32] X. Dai, B.C. Heng, Y. Bai, F. You, X. Sun, Y. Li, Z. Tang, M. Xu, X. Zhang, X. Deng, Restoration of electrical microenvironment enhances bone regeneration under diabetic conditions by modulating macrophage polarization, Bioact. Mater. 6 (2020) 2029–2038.

[33] A.S. Timin, A.R. Muslimov, M.V. Zyuzin, O.O. Peltek, T.E. Karpov, I.S. Sergeev, A. I. Dotsenko, A.A. Goncharenko, N.D. Yolshin, A. Sinelnik, Multifunctional scaffolds with improved antimicrobial properties and osteogenicity based on piezoelectric electrospun fibers decorated with bioactive composite microcapsules, ACS Appl. Mater. Interfaces 10 (2018) 34849–34868.

[34] T. Zheng, H. Zhao, Y. Huang, C. Gao, X. Zhang, Q. Cai, X. Yang, Piezoelectric calcium/manganese-doped barium titanate nanofibers with improved osteogenic activity, Ceram. Int. 47 (2021) 28778–28789.

[35] M. Hu, F. Xiao, Q.F. Ke, Y. Li, X.D. Chen, Y.P. Guo, Cerium-doped whitlockite nanohybrid scaffolds promote new bone regeneration via SMAD signaling pathway, Chem. Eng. J. 359 (2019) 1–12.

[36] Z. Yuan, Z. Wan, C. Gao, Y. Wang, J. Huang, Q. Cai, Controlled magnesium ion delivery system for *in situ* bone tissue engineering, J. Contr. Release 350 (2022) 360–376.

[37] A. Das, D. Pamu, A comprehensive review on electrical properties of hydroxyapatite based ceramic composites, Mat. Sci. Eng. C-Mater. 101 (2019) 539–563.

[38] V.K. Kaliannagounder, N.P.M.J. Raj, A.R. Unnithan, J. Park, S.S. Park, S.J. Kim, C. H. Park, C.S. Kim, A.R.K. Sasikala, Remotely controlled self-powering electrical stimulators for osteogenic differentiation using bone inspired bioactive piezoelectric whitlockite nanoparticles, Nano Energy 85 (2021), 105901.

[39] F. Liu, C. Vyas, G. Poologasundarampillai, I. Pape, S. Hinduja, W. Mirihanage, P. Bartolo, Structural evolution of PCL during melt extrusion 3D printing, Macromol. Mater. Eng. 303 (2018), 1700494.

[40] D. Liu, W. Nie, D. Li, W. Wang, L. Zheng, J. Zhang, J. Zhang, C. Peng, X. Mo, C. He, 3D printed PCL/SrHA scaffold for enhanced bone regeneration, Chem. Eng. J. 362 (2019) 269–279.

[41] S.T. Ho, D.W. Hutmacher, Application of micro CT and computation modeling in bone tissue engineering, Comput. Aided Des. 37 (2005) 1151–1161.

[42] Y. Zhang, H. Leng, Z. Du, Y. Huang, X. Liu, Z. Zhao, X. Zhang, Q. Cai, X. Yang, Efficient regeneration of rat calvarial defect with gelatin-hydroxyapatite composite cryogel, Biomed. Mater. 15 (2020), 065005.

[43] X. Zhang, W. Liu, J. Liu, Y. Hu, H. Dai, Poly-ε-caprolactone/whitlockite electrospun bionic membrane with an osteogenic–angiogenic coupling effect for periosteal regeneration, ACS Biomater. Sci. Eng. 7 (2021) 3321–3331.

[44] Y. Yang, H. Wang, H. Yang, Y. Zhao, J. Guo, X. Yin, T. Ma, X. Liu, L. Li, Magnesium-based whitlockite bone mineral promotes neural and osteogenic activities, ACS Biomater. Sci. Eng. 6 (2020) 5785–5796.

[45] W.B. Lee, C. Wang, J.H. Lee, K.J. Jeong, Y.S. Jang, J.Y. Park, M.H. Ryu, U.K. Kim, J. Lee, D.S. Hwang, Whitlockite granules on bone regeneration in defect of rat calvaria, ACS Appl. Bio Mater. 3 (2020) 7762–7768.

[46] M. Sun, G. Chi, P. Li, S. Lv, J. Xu, Z. Xu, Y. Xia, Y. Tan, J. Xu, L. Li, Effects of matrix stiffness on the morphology, adhesion, proliferation and osteogenic differentiation of mesenchymal stem cells, Int. J. Med. Sci. 15 (2018) 257–268.

[47] T. Wang, S.S. Nanda, G.C. Papaefthymiou, D.K. Yi, Mechanophysical cues in extracellular matrix regulation of cell behavior, Chembiochem 21 (2020) 1254–1264.

[48] M. Kaur, K. Singh, Review on titanium and titanium based alloys as biomaterials for orthopaedic applications, Mat. Sci. Eng. C-Mater. 102 (2019) 844–862.

[49] W. Jing, D. Zuo, Q. Cai, G. Chen, L. Wang, X. Yang, W. Zhong, Promoting neural transdifferentiation of BMSCs via applying synergetic multiple factors for nerve regeneration, Exp. Cell Res. 375 (2019) 80–91.

[50] Y. Tai, S. Yang, S. Yu, A. Banerjee, N.V. Myung, J. Nam, Modulation of piezoelectric properties in electrospun PLLA nanofibers for application-specific self-powered stem cell culture platforms, Nano Energy 89 (2021), 106444.

[51] Y. Zhang, S. Chen, Z. Xiao, X. Liu, C. Wu, K. Wu, A. Liu, D. Wei, J. Sun, L. Zhou, Magnetoelectric nanoparticles incorporated biomimetic matrix for wireless electrical stimulation and nerve regeneration, Adv. Healthc. Mater. 10 (2021), 2100695.

[52] M. Hoop, X.Z. Chen, A. Ferrari, F. Mushtaq, G. Ghazaryan, T. Tervoort, D. Poulikakos, B. Nelson, S. Pané, Ultrasound-mediated piezoelectric differentiation of neuron-like PC12 cells on PVDF membranes, Sci. Rep. 7 (2017) 1–8.

[53] Y. Gao, Z. Yuan, X. Yuan, Z. Wan, Y. Yu, Q. Zhan, Y. Zhao, J. Han, J. Huang, C. Xiong, Bioinspired porous microspheres for sustained hypoxic exosomes release and vascularized bone regeneration, Bioact. Mater. 14 (2022) 377–388.

[54] Y. Zhang, Z. Du, D. Li, Z. Wan, T. Zheng, X. Zhang, Y. Yu, X. Yang, Q. Cai, Catalpol modulating the crosstalking between mesenchymal stromal cells and macrophages via paracrine to enhance angiogenesis and osteogenesis, Exp. Cell Res. 418 (2022), 113269.

[55] Y. Huang, Z. Du, K. Li, W. Jing, P. Wei, B. Zhao, Y. Yu, Q. Cai, X. Yang, Ros-scavenging electroactive polyphosphazene-based core–shell nanofibers for bone regeneration, Adv. Fiber. Mater. 4 (2022) 894–907.

[56] L. Zhang, Y. Yu, C. Joubert, G. Bruder, Y. Liu, C.C. Chang, M. Simon, S.G. Walker, M. Rafailovich, Differentiation of dental pulp stem cells on gutta-percha scaffolds, Polymers 8 (2016) 193–201.
[57] F. Zhao, W. Xie, W. Zhang, X. Fu, W. Gao, B. Lei, X. Chen, 3D printing nanoscale bioactive glass scaffolds enhance osteoblast migration and extramembranous osteogenesis through stimulating immunomodulation, Adv. Healthc. Mater. 7 (2018), 1800361.
[58] R. Detsch, A.R. Boccaccini, The role of osteoclasts in bone tissue engineering, J. Tissue. Eng. Regen. M. 9 (2015) 1133–1149.
[59] P. Gomes, M. Fernandes, Rodent models in bone-related research: the relevance of calvarial defects in the assessment of bone regeneration strategies, Lab. Anim. 45 (2011) 14–24.
[60] D. Khare, B. Basu, A.K. Dubey, Electrical stimulation and piezoelectric biomaterials for bone tissue engineering applications, Biomaterials 258 (2020), 120280.
[61] C. Shuai, W. Yang, P. Feng, S. Peng, H. Pan, Accelerated degradation of HAP/PLLA bone scaffold by PGA blending facilitates bioactivity and osteoconductivity, Bioact. Mater. 6 (2021) 490–502.
[62] H. Takahashi, Y. Numamoto, J. Tani, K. Matsuta, J. Qiu, S. Tsurekawa, Lead-free barium titanate ceramics with large piezoelectric constant fabricated by microwave sintering, Jpn. J. Appl. Phys. 45 (2005) L30.
[63] W. Wang, S. Itoh, Y. Tanaka, A. Nagai, K. Yamashita, Comparison of enhancement of bone ingrowth into hydroxyapatite ceramics with highly and poorly interconnected pores by electrical polarization, Acta Biomater. 5 (2009) 3132–3140.
[64] Z. Li, X. Zhang, J. Ouyang, D. Chu, F. Han, L. Shi, R. Liu, Ca^{2+}-supplying black phosphorus-based scaffolds fabricated with microfluidic technology for osteogenesis, Bioact. Mater. 6 (2021) 4053–4064.
[65] Z. Zhang, Z. Hao, C. Xian, Y. Fang, B. Cheng, J. Wu, J. Xia, Neuro-bone tissue engineering: multiple potential translational strategies between nerve and bone, Acta Biomater. xx (2022), https://doi.org/10.1016/j.actbio.2022.09.023.
[66] Y.X. Ma, K. Jiao, Q.Q. Wan, J. Li, M.Y. Liu, Z.B. Zhang, W. Qin, K.Y. Wang, Y. Z. Wang, F.R. Tay, L.N. Niu, Silicified collagen scaffold induces semaphorin 3A secretion by sensory nerves to improve *in-situ* bone regeneraion, Bioact. Mater. 9 (2022) 475–490.
[67] Q.Q. Wan, K. Jiao, Y.X. Ma, B. Gao, Z. Mu, Y.R. Wang, Y.H. Wang, L. Duan, K. H. Xu, J.T. Gu, J.F. Yan, J. Li, M.J. Shen, F.R. Tay, L.N. Niu, Smart, biomimetic periosteum created from the cerium (III, IV) oxide-mineralized eggshell membrane, ACS Appl. Mater. Interfaces 14 (2022) 14103–14119.